Head check resistance of B320 bainitic rail steel grade

Thibault Lesage, Marie-Noëlle Avettand-Fènoël, David Balloy, S. Assaf, F. Cristofari, P. Secordel

Version of Record: https://www.sciencedirect.com/science/article/pii/S2352492822001350
Manuscript_4727f76bb0330d2982961dad3b756c6d

Head check resistance of B320 bainitic rail steel grade.

T. Lesage[1-2*], M.N. Avettand-Fènoël[2], D. Balloy[2], S. Assaf[1], F. Cristofari[3], P. Secordel[3]

[1] Institut de Recherche Technologique RAILENIUM, F-59300, Famars, France
[2] Univ. Lille, CNRS, INRAE, Centrale Lille, UMR 8207 - UMET - Unité Matériaux et Transformations, F-59000 Lille, France
[3] Saarstahl Rail, 164 rue du Maréchal Foch, BP 10166, 57705 Hayange Cedex, France

Corresponding author: thibault.lesage@railenium.eu

Abstract

This work focuses on the degradation mechanisms of a B320 carbide-free bainitic steel grade rail and of its weld after laboratory tests. The microstructure of the tested rails is investigated, focusing mainly on retained austenite. The Head Check resistance of B320 grade base material is high, notably due to the TRansformation Induced Plasticity (TRIP) effect, inducing a reduction in crack propagation speed. Inside the Heat Affected Zone, a few Head Check defects have been detected and are attributed to a lower retained austenite content coming with a higher Martensite-Austenite Compound content prior to rail testing. In this zone, the transformation process from austenite to martensite following TRIP effect is less pronounced. A novel degradation mechanism is proposed considering the phases contribution in the deformation process of B320 carbide free steel grade.

Graphical abstract

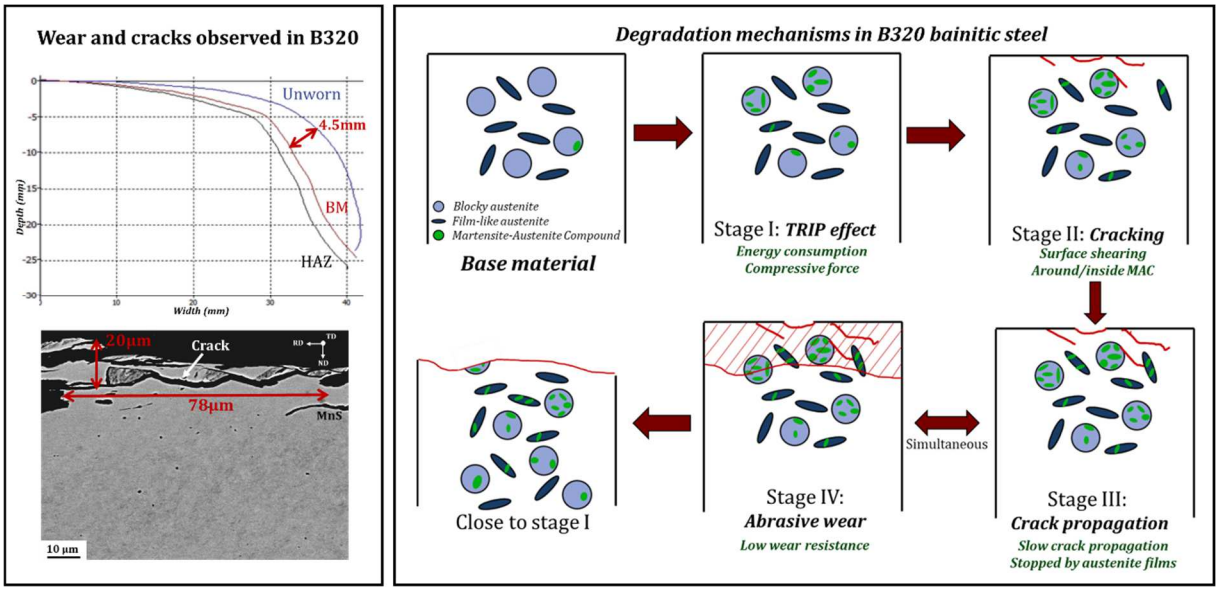

Keywords: Carbide-free bainitic steel; microstructure; head check defects; TRIP effect

1. Introduction

In the railway sector, improvements are made on the network capacity, its reliability and life span while reducing its maintenance operations and costs. The tracks are subjected to high stresses that cause rail damage, including cracks which may eventually lead to fracture of rails [1]. This involves serious safety issues and high maintenance costs which have to be avoided. In Europe, most of the rail network is equipped with rails rolled from pearlitic steel grades, such as R260, R350HT or MHH (Maximum Head Hardness) grades [2–4]. These steels are prone to Rolling Contact Fatigue (RCF), and more specifically to Head Check (HC) defects [2]. HC defects are cracks found at the gauge corner of the outer rail. Such defects are usually clustered at uniform intervals and are mostly observed on curved tracks of radii less than 3000 m as well as in switches and crossings [5].

Under mechanical solicitation, the rails present plastic deformation located at its surface and subsurface. In pearlitic steel rail, cementite lamellae break down at the sub-surface and reorient themselves in sliding direction [3]. This in turn leads to a grain refinement [6,7] in close surface, followed by work hardening [3]. Cementite laths are then progressively dissolved [8,9], which leads to an increase of carbon content in the matrix [10]. This increase of carbon content often induces the formation of carbides, as well as a hard and brittle White Etching Layer (WEL) [11,12]. While WEL is not a necessary condition for crack occurrence, it lowers fracture toughness, which make it a preferential crack initiation site [13]. Once WEL is formed, squat and head check are likely to occur. Head check cracks will propagate along the microstructure, increasing the risks of rail failure. Grinding or rail replacement every few years becomes mandatory to lower the risks of train derailment. Wear and head check resistance of pearlitic steels can be improved [14] by decreasing the size of pearlite colonies [15], the interlamellar spacing [16] and the size of prior austenite grains [17]. This overall microstructure refinement is usually achieved by increasing the carbon content [18] of pearlitic steels. However, high carbon content is detrimental to the weldability and toughness of pearlitic steel. Thus, it is believed that the mechanical properties of pearlitic rail steels are close to their theoretical limit with current chemistries and processing techniques [2,19,20].

Therefore, novel solutions are being investigated. Carbide-free bainitic (CFB) steels are one of the promising materials that could be used to replace pearlitic steel rails, especially in large curves, switches, and crosses. These rails present an outstanding resistance to RCF, and especially to HC defects. HC resistance is most often higher in CFB compared to pearlitic steels and cracks are not commonly found, even close to the surface [21,22].

One of the key parameter attributed to the elevated HC resistance of CFB is linked to retained austenite [23]. Retained austenite (RA) can be found in two distinct shapes in bainitic steels: film-like austenite and blocky austenite. Film-like austenite is a very thin region (typical width of few nanometers), mostly observed between parallel sub-units or plates or sheaves of bainitic ferrite [23]. This film-like austenite usually presents a high local carbon content, going as high as 7.5 at % [24],

while blocky austenite typically presents a carbon content close to 5.5 at% [24]. This high carbon content, along with high specific surface area [25], provides a high mechanical stability [26], at the expense of a low thermal stability [27,28]. Blocky austenite is commonly found in blocks of a few micrometers width. Its lower mechanical stability, associated with lower carbon content [28], leads to the transformation of blocky austenite into martensite, following TRansformation Induced Plasticity (TRIP) effect [29]. TRIP effect is a well-known phenomenon in steel strengthening mechanisms [30–33]. Due to the mechanical solicitation existing in railways, up to 90% of RA is transformed into martensite close to the surface [34,35]. This transformation concerns essentially blocky austenite, whose mechanical stability is lower, but is also expected in lesser proportion in film-like austenite.

The effect of austenite on RCF resistance is not trivial. Film-like RA lowers crack propagation rate by adding austenite-ferrite interfaces that are highly energy consuming to cross [36]. It also induces localized TRIP effect at crack tip, leading to small crack closure [37]. Lowering inter-lath distance between austenite films increases the amount of barriers to crack propagation, which is beneficial for wear and RCF resistance [3,38]. Blocky austenite presents a lower mechanical stability, and therefore induces a larger amount of TRIP, which actively participates to crack closure effect. However, newly formed martensite is brittle and might lead to an increased crack propagation speed through preferential crack propagation path [39]. Moreover, due to stress concentration inside newly formed martensite, there are risks of microcracks formation inside martensite or at the interface of martensite and bainitic ferrite [40,41].

The present work aims to understand the damage mechanisms during RCF in a carbide-free bainitic steel. To do so, thorough investigations were performed to deeper understand the damage mechanisms of CFB steels, paying special attention to the role of austenite. Thus, laboratory rig tests were performed to study the RCF resistance of B320 CFB steel grade. The evolution of retained austenite content is followed inside several regions of the rail, namely base material, fusion zone and Heat Affected Zone (HAZ). Heat Affected Zone is an important part of the rails since rail failures commonly occur inside this zone. The comparison of this region, with a distinct thermal history and thus a different microstructure, enables to study the degradation behavior of this carbide-free rail. A degradation mechanism is finally proposed for this steel in railways application.

2. Material and methods

2.1. Initial rails

Rail steels used in this study are B320 carbide-free bainitic steel grade, whose chemical composition and mechanical properties are given in Table 1 and Table 2, respectively. For comparative purpose, a R260 pearlitic steel grade (Table 1) has also been considered. The composition of the filler material used during welding, *i.e.* the composition of the fusion zone, is also indicated in Table 1.

The rails were industrially produced by Hayange (France) rail mill using initial rectangular section bars (blooms) heated up, hot rolled and air cooled down up to ambient temperature. These blooms were then shaped into Vignole rails with initial 60E2 profile.

In CFB, the formation of cementite is suppressed by the addition of about 1.5 wt% Si [42–44]. However, while cementite is not prone to be formed from retained austenite, other carbides precipitation is still possible in the bainitic ferrite [45] or martensite [46,47].

Table 1: Chemical composition intervals (in wt.%) of B320 bainitic steel and R260 pearlitic steel as indicated by Liberty Rail Hayange. The composition of the fusion zone coming from aluminothermic welding is measured by EDS

Grade	C	Mn	Si	Cr	Mo	V	S	Al	P	Fe
B320	0.13-0.27	1.35-1.75	1.00-1.50	0.30-0.70	0.10-0.30	0.10-0.30	≤0.025	≤0.004	≤0.025	Bal.
R260	0.60-0.82	0.65-1.25	0.13-0.60	≤0.15		≤0.030	≤0.030	≤0.004	≤0.030	Bal.
Fusion zone	?	0.3	1.9	2.6						Bal.

Table 2: Mechanical properties of B320 bainitic and R260 pearlitic steel grades as indicated by Liberty Rail Hayange.

Grade	Rp0.2 (MPa)	UTS (MPa)	A (%)	K1C (MPa. √m)	Hardness (HB)	da/dN (m/Gcycles)	
						ΔK = 10 MPa√m	ΔK = 13,5 MPa√m
B320	869 ± 61	1123 ± 24	14.7 ± 1.4	41 ± 5	341 ± 16	17	55
R260	520 ± 19	960 ± 57	12.0 ± 2.3	36 ± 5	279 ± 18	9	26

Aluminothermic welds were performed on the B320 rails before testing, as shown in Figure 1.

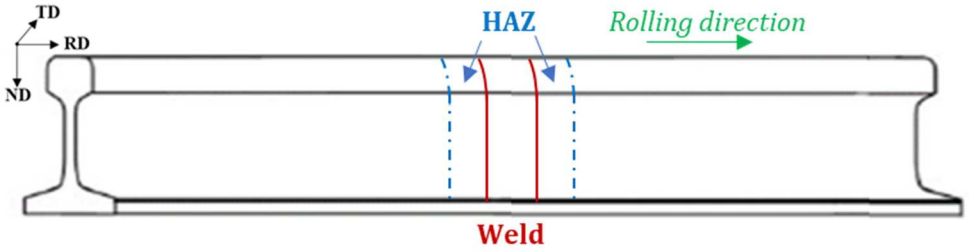

Figure 1 : Welded Vignole 60E2 profile rails.

Welds were performed by Goldschmidt, Germany, following Thermit® SoW-5 process. Thermit welding is based on an exothermic chemical reaction, which involves the reduction of a metal oxide, usually iron oxide, by aluminum, as shown in the reaction (1) [48].

$$Fe_2O_3 + 2\ Al \rightarrow Al_2O_3 + 2\ Fe \quad + \Delta H \qquad (1)$$

The molds were preheated to about 500°C, and the crucible was prepared with the filler metal whose chemical composition is supplied in Table 1. An ignitor such as barium peroxide started the aluminothermic reaction, achieving temperatures up to 2500°C. Once the reaction finished and the weld cooled down to 1100-1200°C, the mold and crucible were removed and the weld was left to cool [48]. Thermit® SoW-5 welding is specifically designed for railways application. One of its main advantages is the very short pre-heating period (3 to 6 min) [49].

The welding process leads to the formation of distinct zones: the Fusion Zone (FZ) and the Heat Affected Zone (HAZ) surrounding it.

2.2. Rig test

Rig tests (Figure 2) were performed on Deutsche Bahn Systemtechnik's wheel-rail test rig A, located at Kirchmöser (Germany). Rig tests were performed on rails of 3.2 meters for 100 000 cycles, each cycle being composed of two parts: loading and unloading. During the loading part, the rail moved following the rolling direction at a constant speed of 2 m/s. During this translation, both a vertical load, representing the tonnage, and a constant lateral force of 10 kN were applied. To approximate the conditions of curve negotiation, the wheel ran against the rail with a 3 mrad angle of attack. During the unloading part, both the vertical and lateral forces were removed, and the wheel was raised from the rail to ensure a testing scenario corresponding to a solicitation along a single direction. This test, which leads to a solicitation mainly located on the gauge corner compared to service rail for identical tonnage, is designed to favor head check defects appearance. While the 100 000 cycles correspond to approximately 2.4 MGT, wear and head check in gauge corner are way more pronounced as this tonnage suggests. Head check defects observed after rig test in R260 have been compared to service rails. Such tested pearlitic rails present a HC defects severity similar to the one observed in service rails after 100 to 300 MGT.

Monoblock wheels made of ER8 steel were used as counter materials for rig tests.

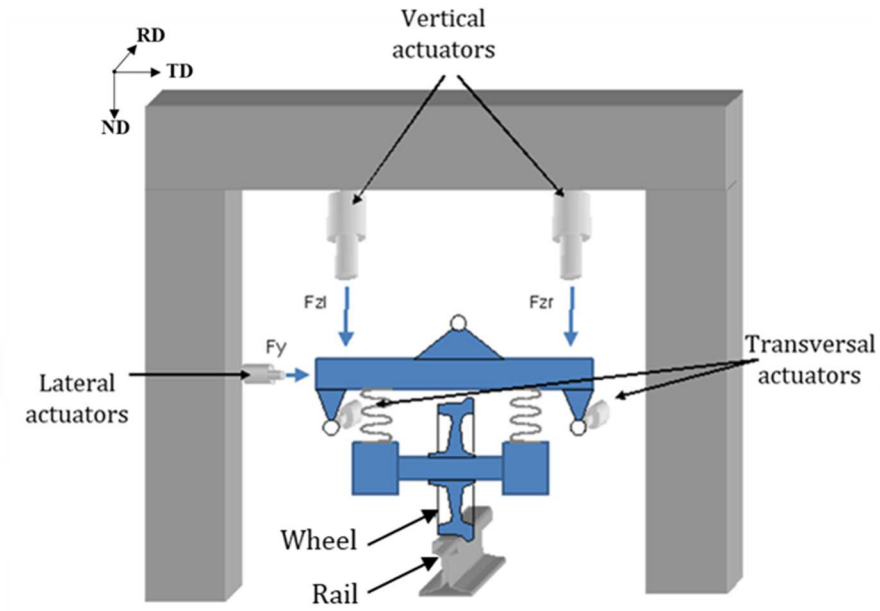

Figure 2 : Scheme of Deutsche Bahn Systemtechnik's wheel-rail rig test A.

Table 3 : Summary of test conditions during rig test A. Identical test conditions were used for both B320 and R260 steel grades.

Load cycles	Static load (kN)	Lateral force (kN)	Contact angle (mrad)	Maximum speed (m/s)	Time frame (days)
100 000	120	10	3	2	8

An oxide layer of about 10 µm has been observed due to the rail storage after rig test. The removal of these oxides leads to the suppression of a few supplementary micrometers under the surface. Thus, it

has been chosen to keep these oxides to preserve as much information as possible close to the contact surface.

2.3. Samples preparation and characterization techniques

The 3-D profiles of the tested rails were measured using the Scorpion™ 3-D laser measurement system. Profilanalyzer™ 2.2 software was used to create a 3-D model of the running surface, with a measurement uncertainty of 0.05 mm. From these 3-D maps, a 2-D averaged map is produced, indicating the average surface profile along the measured distance (length = 300 mm).

Most of the quantitative analyses were carried out *via* microstructural characterization techniques. Systematic polishing was performed using grid papers grad 180, 300, 500, 800, 1200, 2400, followed by finish polishing using 6 µm, 3 µm, 1 µm and ¼ µm diamond paste. This metallographic preparation was followed by etching using a Picral solution with 0.5% HCl for optical microscopy (OM) and scanning electron microscopy (SEM) investigations . For electron back scattered diffraction (EBSD) and X-Ray Diffraction (XRD) investigations, etching is replaced by mechanical polishing using VibroMet 2 vibratory polisher. A solution of 30% Oxide Polishing Suspension (OPS) with colloidal silica – 70 % ethylic alcohol was used at 100% vibration for 1 hour followed by 36 hours at 10% vibration. XRD samples are prepared using the same preparation method as for EBSD samples, skipping papers grade 180 to lower the risks of phase transformation.

Observations were performed with a light Microscope Zeiss Axioplan®, as well as a Hitachi SU5000 scanning electron microscope with secondary electron (SE) and backscattered electron (BSE) modes. Energy Dispersive X-ray analysis (EDX) was used for chemical identification at a microscopic scale. EBSD and Transmission Kikuchi Diffraction (TKD) are performed to have crystal orientations at the micrometric and submicrometric scales.

EBSD measurements are carried out using Oxford Instruments Symmetry® camera and AZtec acquisition software. EBSD data post processing is performed using ATEX on-line free software [50]. EBSD samples are tilted at 70° from camera angle, with a working distance of 15 mm and a voltage of 20 kV. All EBSD investigations on deformed samples are performed with a 70 nm step size, while base material investigations are realized with a 150 nm step size, to have wider ranges of investigation. EBSD analyses are performed on cross sections of the rails, in both the undeformed condition (not solicited rail, measurements at 1300 µm depth) and the deformed condition (adjacent to contact surface). Rolling direction, when applicable, is always from left to right of EBSD image. TKD and Transmission Electron Microscopy measurements are performed on thin foils parallel to the contact surface. Considered depth at which the thin foils have been sampled is indicated in each figure.

XRD analyses were performed with a Diffractometer X'Pert Pro® from Philips-Panalytical in Bragg-Brentano configuration, using a Kα cobalt wavelength at 0.1789 nm and with a Kβ iron filter. It allows quantitative phase quantification, complementary to EBSD investigations. Thin foils for TEM were obtained by mechanically grounding thin sections up to a thickness of 50-100 µm, prior to

electropolishing until perforation using a 5 vol.% perchloric acid in methanol solution as described in Devanathan *and al.* [51]. TEM analyses were carried out on a FEI G2000 Tecnai instrument, using a Field Electron Gun (FEG) electron source and allow observations at nanoscale. Finally, TEM orientation imaging (ASTAR) is performed with NanoMEGAS ASTAR® instrument, with a spot size of 9, corresponding to a resolution of 10 nm to 15 nm.

3. Results

Wheel-rail contact leads to severe sub-surface microstructural modifications of the rails. The wear and head check resistance after rig test are investigated. Microstructural investigations provide insights of the mechanisms occurring inside B320 steel grade.

3.1. Rail damages at macroscopic scale

After rig test, rail damage is investigated considering the evolution of the rail profile and material loss from initial to final configuration in both the base material and the heat affected zone. The head of the B320 bainitic rail is severely damaged and significant material loss is noticed (Figure 3a) compared to R260 pearlitic rail (Figure 3b). The mass loss per meter of rail is then calculated considering the mass density of the rail (Table 4).

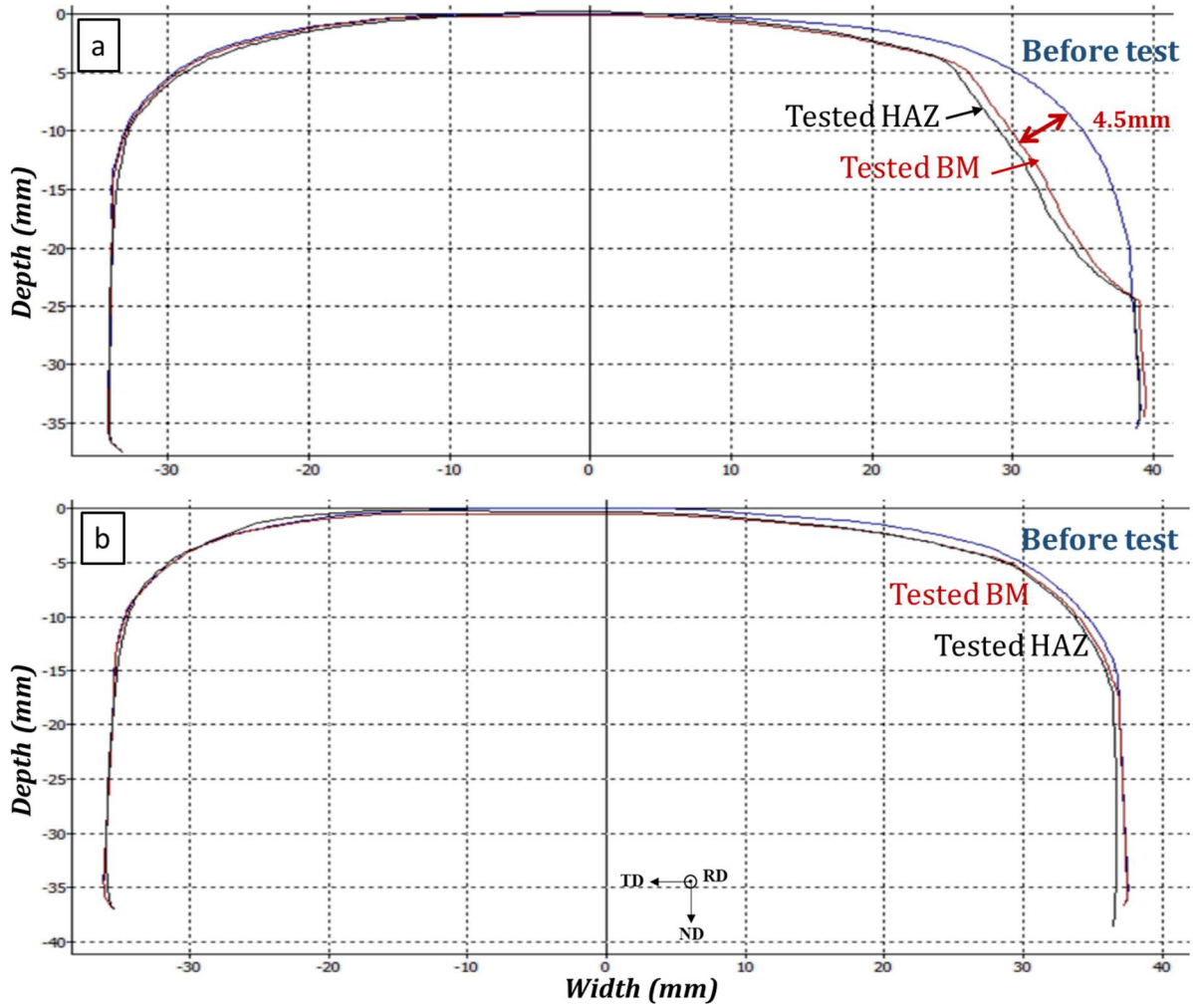

Figure 3: Rail profiles before and after rig test for a- B320 bainitic steel b- R260 pearlitic steel. BM = Base Material, HAZ = Heat Affected Zone

Table 4: Damage of R260 pearlitic and B320 bainitic steel rails.

	R260		B320	
	Base material	HAZ	Base material	HAZ
Transverse surface loss (mm^2)	28	66	117	147
Material loss ($g.m^{-1}$)	217	512	909	1141
Material loss rate ($mg.s^{-1}.m^{-1}$)	1.3	3.1	5.5	6.8

The material loss rate of bainitic steel rail B320 after rig test is 2 to 4 times greater than the one observed in R260 pearlitic steel, indicating a lower wear resistance of B320. Material loss rate is higher inside the HAZ compared to the base material for both R260 and B320 grades.

However, the occurrence of HC cracks in close surface has been investigated on transverse cross sections of damaged HAZ and base material (Table 5).

Table 5 : Formation of HC cracks for R260 pearlitic and B320 bainitic steel rails.

	R260		B320	
	Base material	HAZ	Base material	HAZ
Crack existence	Crack network	Crack network	No crack	Rare cracks
Maximum crack length (mm)	< 15	15.2	0	80.10^{-3}

B320 did not present any crack in the base material. Only rare micro-cracks could be seen in the HAZ of B320 grade, as seen in Figure 4.a. All the HC cracks were seen in the HAZ between 1 and 3 cm along the rolling direction from the fusion zone, most of them being located at 2 cm from the fusion zone. The few observed microcracks in the HAZ were found out to be located at less than 20 µm from the surface along the normal direction, with a maximum measured length of 78 µm (Figure 4.a).

Conversely, large cracks and eventually crack networks are observed in R260 along the whole rail (Figure 4.b). As a result, B320 presents a lower wear resistance but significantly higher Head Check (HC) resistance compared to R260. Its applicability thus differs from classical R260 pearlitic steel and must be used in places where RCF resistance is prevalent compared to wear resistance.

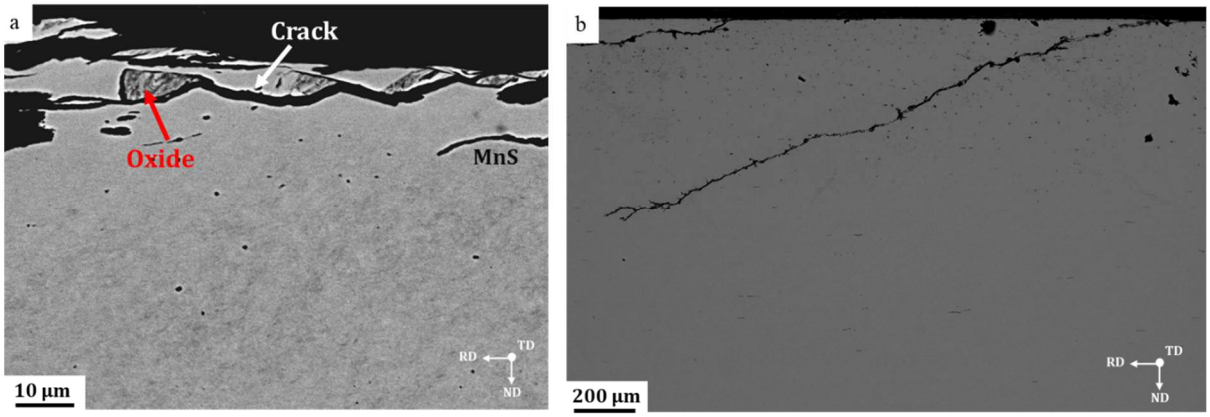

Figure 4: a- Longest crack observed in B320 CFB rail, observed in the HAZ at 2 cm from fusion zone and b- typical crack formed by head check in R260 pearlitic steel

The length and depth of observed microcracks in B320 (Figure 4.a) are low compared to the material loss, where several millimeters are removed from the initial profile at the gauge corner (Table 4). Seeing the small dimensions of cracks formed by HC in B320, they might be susceptible to be hindered by the elevated wear observed. Thus, the extremely rare occurrence of HC cracks after rail testing may be partly explained by this competition between wear and HC defects.

However, while only a few microcracks could be observed in the HAZ, their very existence shows that this zone is sensitive to HC in B320 bainitic rails, and previously proposed phenomenon is not sufficient to explain the near absence of HC cracks, since the material loss is slightly higher compared to the base material (Table 4) in this area. According to the positioning along the rail (base material or HAZ), there might be a different predominant damage mechanisms according to the local microstructure.

This work now focuses on understanding the reasons underneath the lower HC resistance of the HAZ compared to the base material. To do so, the microstructure of the HAZ at 2 cm from the fusion zone is especially compared to the one observed in the base material, both prior rail testing and after rig test.

3.2. Initial microstructure

3.2.1. Base material

B320 Carbide Free Bainitic steel is mainly composed of bainitic ferrite (in blue in Figure 5.b) and retained austenite (in red in Figure 5.b). Prior Austenite Grains (PAG) are observed along the microstructure (Figure 5.a). It also presents some Martensite-Austenite Compounds (MAC) which are intertwined areas where both martensite and austenite are to be found. Martensite and bainitic ferrite are both indexed in b.c.c. by EBSD investigations. Thus, the distinction between these two phases remains unclear with these methods. However, martensite is found inside MAC, which induces a lower indexing quality in this region due to the superposition of f.c.c. patterns and b.c.c. patterns. As a result, these MAC appear dark in band contrast, which allow their quantification by ImageJ software.

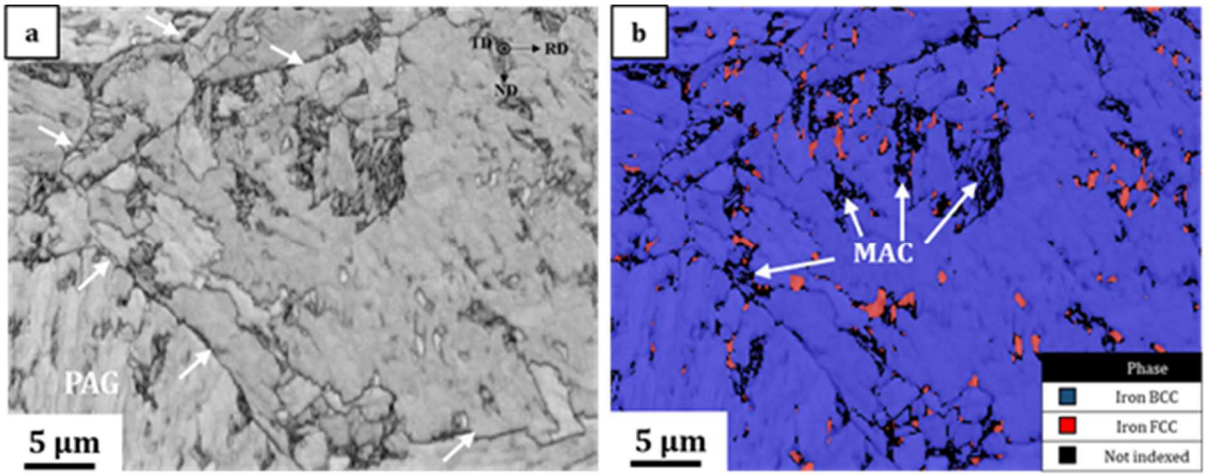

Figure 5: Transverse microstructure of the B320 grade base material, showing bainitic ferrite, retained austenite and Martensite-Austenite Compound (MAC) obtained by EBSD presenting a- index quality map obtained by EBSD and b- EBSD phase map superimposed with index quality map

Retained austenite is either film-like shaped (Figure 6.a), or blocky shaped (Figure 6.b). Blocky austenite is rather equiaxed; its diameter typically ranges from 0.5 to 1.5 µm (assuming a perfectly spherical shape, Figure 6.b). Conversely, film-like austenite is smaller with a 10 to 100 nm width by 1 to 2 µm length (Figure 6.a).

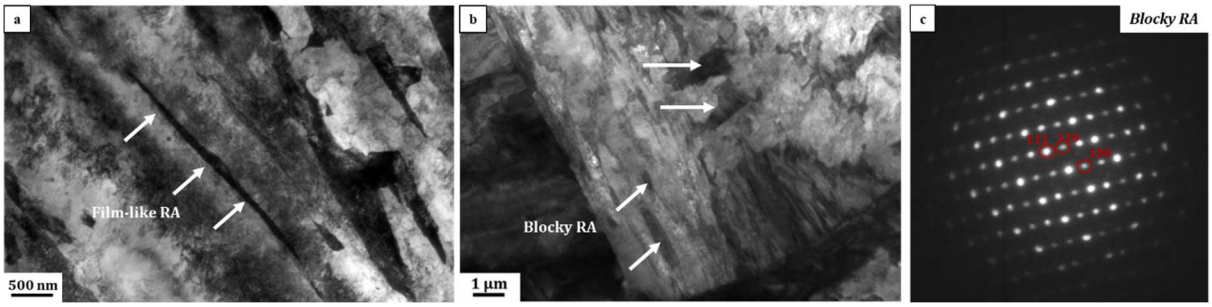

Figure 6: a- Film-like retained austenite, b- blocky retained austenite observed in the initial Heat Affected Zone (TEM) and c- diffraction pattern corresponding to the blocky RA observed in figure b, following [-1 1 0] zone axis.

The microstructure of B320 CFB base material is indicated in Figure 7, and its main features are given in Table 6. The bainitic structure is clearly observed, with bainitic laths inscribed inside bainitic sheaves, itself contained inside a prior austenite grain. Prior austenite grain size is close to 60 µm x 50 µm in the base material (Table 4). Bainitic sheaves and bainitic laths in base material present typical dimensions of 27.4 µm x 9.2 µm and 6.0 µm x 1.9 µm, respectively. The surfacic fraction of retained austenite measured by EBSD is 3.3% inside the base material. MAC content is determined by ImageJ and estimated at around 6.4%. EBSD measurements take only into account blocky austenite, leaving film-like austenite and austenite inside MAC unquantified. Conversely, XRD analyses are believed to measure the total austenite content, including blocky austenite, film-like austenite, and austenite inside MAC. XRD investigations indicates a total of 7.6 vol.% retained austenite inside base material. XRD and EBSD analyses are thus complementary in phase quantifications since they do not consider the same categories of austenite.

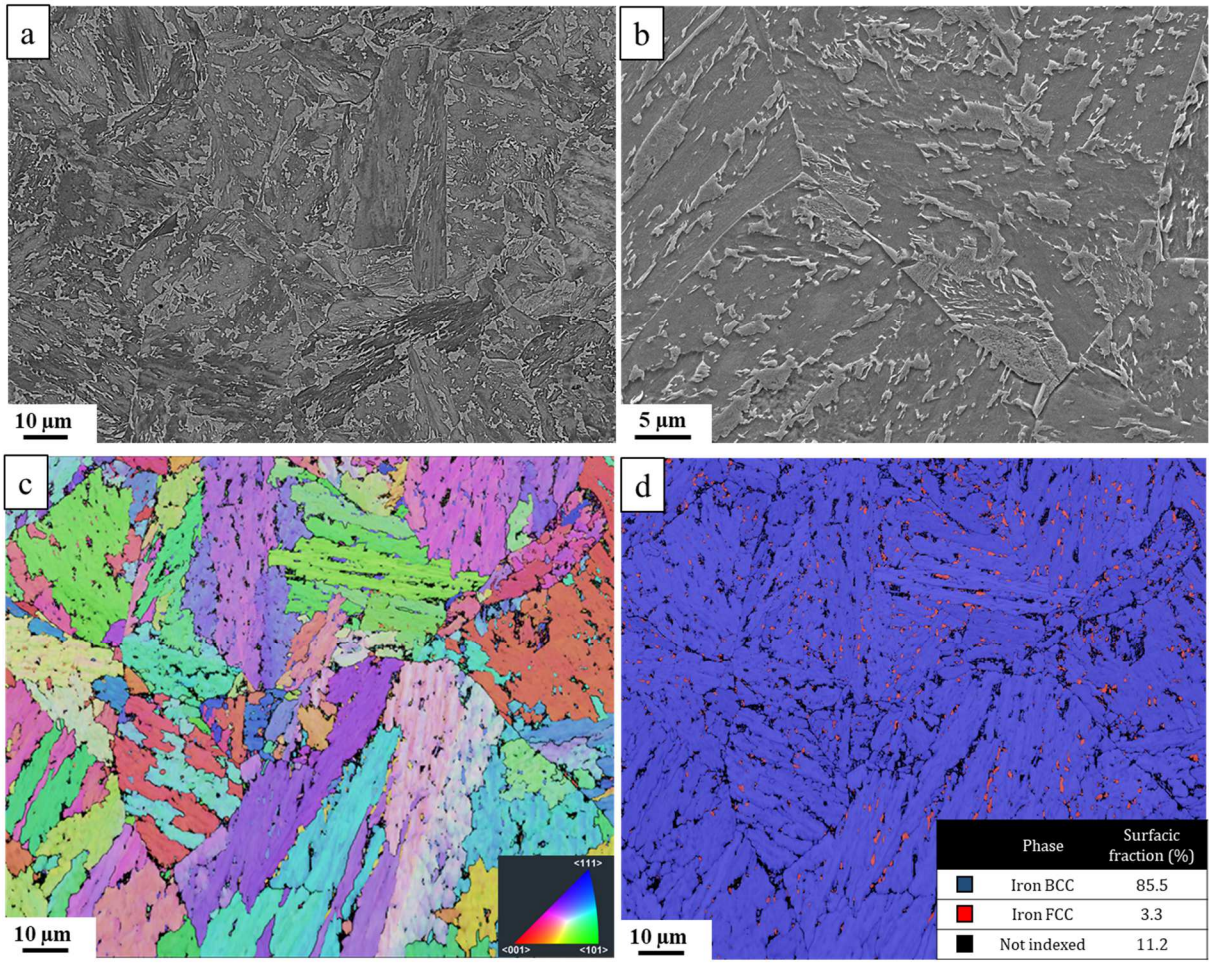

Figure 7: Initial microstructure of the B320 bainitic steel base material (EBSD) in base material a- and b- SEM imaging at different scales, c- orientation mapping following TD coupled with band contrast map, d- corresponding phases map

3.2.2. Fuzion zone and Heat Affected Zone

The microstructure in the fusion zone (Figure 8.a) is coarser compared to that in the base material. Both the bainitic ferrite and the prior austenite grain size dimensions are significantly increased in the Fusion Zone (Table 6). The retained austenite content is higher than in the base material (Table 6), regarding both blocky austenite and global austenite contents.

Figure 8 and Figure 9 are obtained from a single sample, cut along rolling direction prior to rail solicitation. Provided distances correspond to the distance between the end of the fusion zone and the middle of the EBSD scan. The center of the weld is always located at the left side of the EBSD analyses presented on these figures.

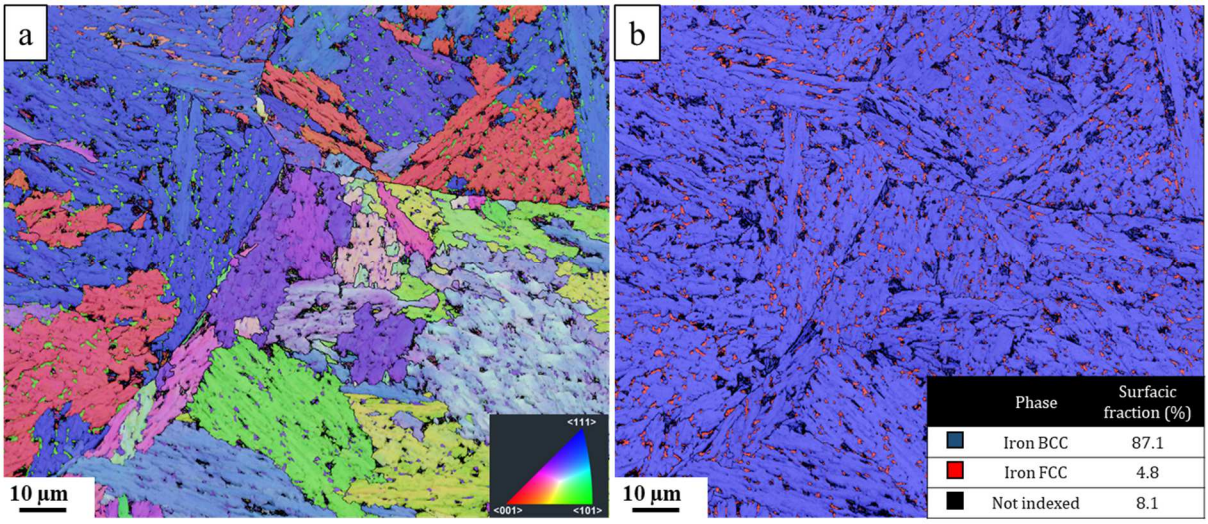

Figure 8: Initial microstructure observed by EBSD of B320 bainitic steel rail in fusion zone a- orientation mapping following TD coupled with band contrast map, b- corresponding phases map

Close to the weld itself, the Heat Affected Zone (HAZ) is observed. Since the thermal history inside this region is highly dependent on the spatial position, several distances from the Fusion Zone along the rolling direction are considered. All analyzes were performed at a depth of 1300 µm (along the normal direction) from the contact surface to ensure repetitive configurations (Figure 9).

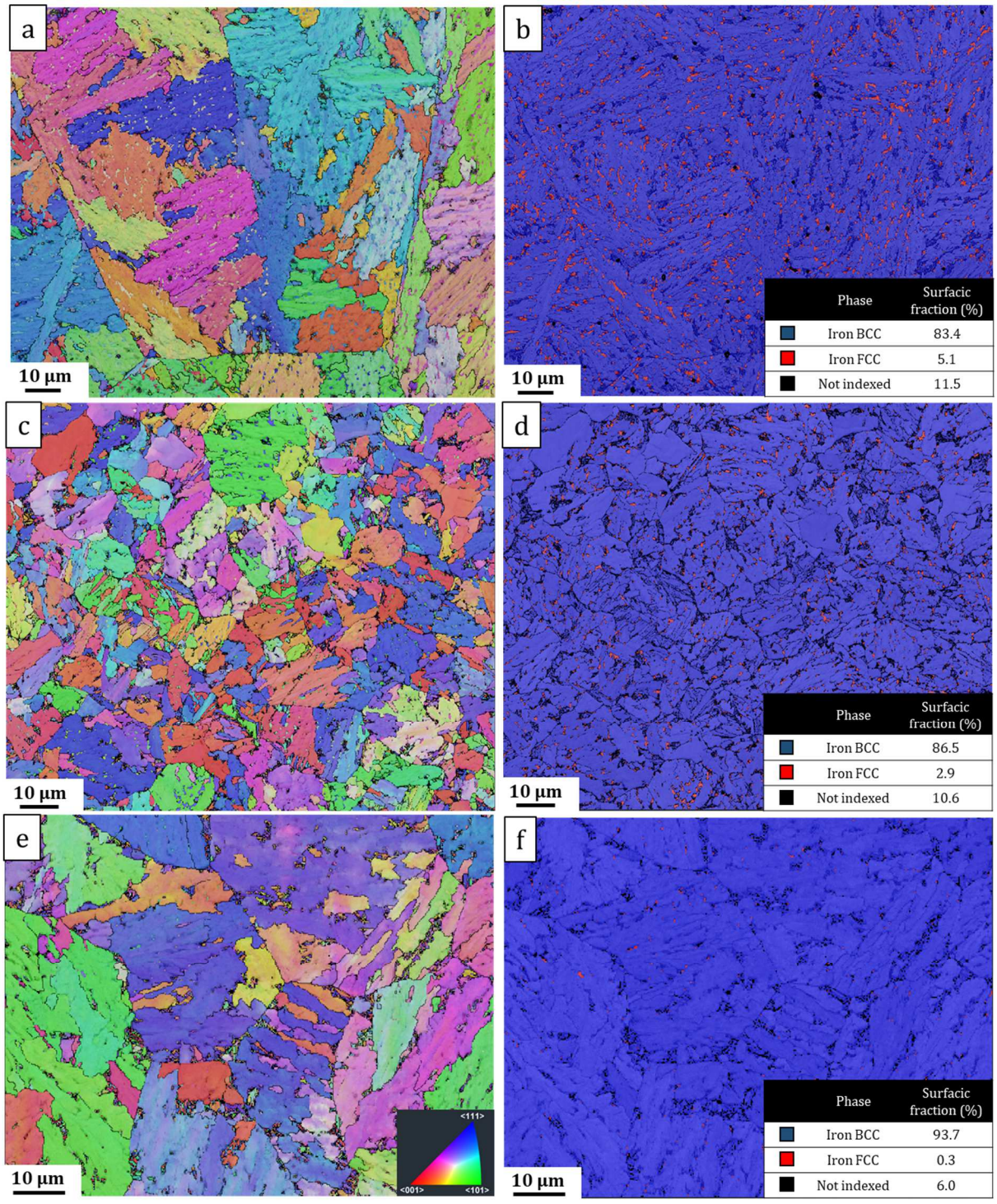

Figure 9: Initial microstructure observed by EBSD: orientation mapping following TD and corresponding phases maps in the heat affected zone at 1300 µm depth from the surface. a-b: at 100 µm, c-d: at 1 cm and e-f: at 2 cm from FZ along the rolling direction.

At 100 µm from the Fusion Zone, a noticeable microstructural coarsening is observed compared to the base material, with prior austenite grain size almost twice bigger, which corresponds to the Coarse Grain Heat Affected Zone (CGHAZ). Conversely, a microstructure refinement (Fine Grain Heat Affected Zone FGHAZ) is observed at a distance of 1 cm from the fusion zone, with an average prior austenite grain diameter as low as 15 µm (Table 6). This PAG size slightly increases at 2 cm from the

fusion zone, with PAG grains of about 25 µm (Table 6), going with very low amount of retained austenite (<0.5% measured by EBSD) and high amount of MAC (8.6% measured by ImageJ), suggesting the Inter Critical Heat Affected Zone (ICHAZ) [52–54]. This region is believed to exhibit some brittle fracture tendency [52] and tends to be detrimental to resistance to cracking [55,56]. Table 6 sums up the main microstructural parameters of the initial microstructure.

Prior austenite grain sizes are determined by scanning electron micrographs observations, coupled with ImageJ software. A minimum of 150 PAG are considered.

Table 6: Summary of initial microstructure phase content (in surfacic content) and geometrical features in the different regions of B320 bainitic steel rail. Blocky austenite content and prior austenite grain sizes are determined by EBSD, MAC content, bainitic laths and sheaves dimensions are determined by EBSD coupled with ImageJ software. Total austenite content is measured by XRD, while film-like austenite dimensions are determined by TEM

	Base Material	HAZ 2 cm	HAZ 1 cm	HAZ 100 µm	Fusion Zone
Blocky austenite (%)	3.3 ± 0.9	0.3 ± 0.2	2.9 ± 0.3	5.1 ± 0.5	4.7 ± 0.8
MAC (%)	6.4 ± 1.2	8.6 ± 1.4	6.8 ± 1.4	5.8 ± 1.1	5.5 ± 1.1
Total austenite (%)	7.6 ± 1.0	3.7 ± 1.0	7.4 ± 1.0	9.0 ± 1.0	9.1 ± 1.0
Blocky austenite diameter (µm)	1.35 ± 0.75	NA	0.65 ± 0.33	1.27 ± 0.19	1.43 ± 0.48
Film-like austenite length and width (nm x nm)	1500 ± 800 x 55 ± 45	2200 ± 700 x 180 ± 70	-	-	-
Bainitic laths length and width (µm x µm)	6.0 ± 1.1 1.9 ± 0.3	6.0 ± 1.5 1.5 ± 0.3	4.0 ± 1.4 1.4 ± 0.2	8.1 ± 2.4 1.7 ± 0.5	11.3 ± 5.0 2.2 ± 0.6
Bainitic sheaves length and width (µm x µm)	27.4 ± 13.4 9.2 ± 5.0	12.5 ± 5.7 3.5 ± 2.6	11.7 ± 3.3 3.3 ± 1.4	26.4 ± 8.0 8.8 ± 4.1	25.0 ± 9.3 15.8 ± 10.2
Prior austenite grain sizes (µm)	55 ± 10	25 ± 15	15 ± 5	100 ± 20	350 ± 40

3.3. Sub-surface microstructural evolution after rig test

3.3.1. Base material

Mechanical solicitation during rig test leads to sub-surface modifications of the tested rail. Resulting microstructure is observed by EBSD and presented in Figure 10.

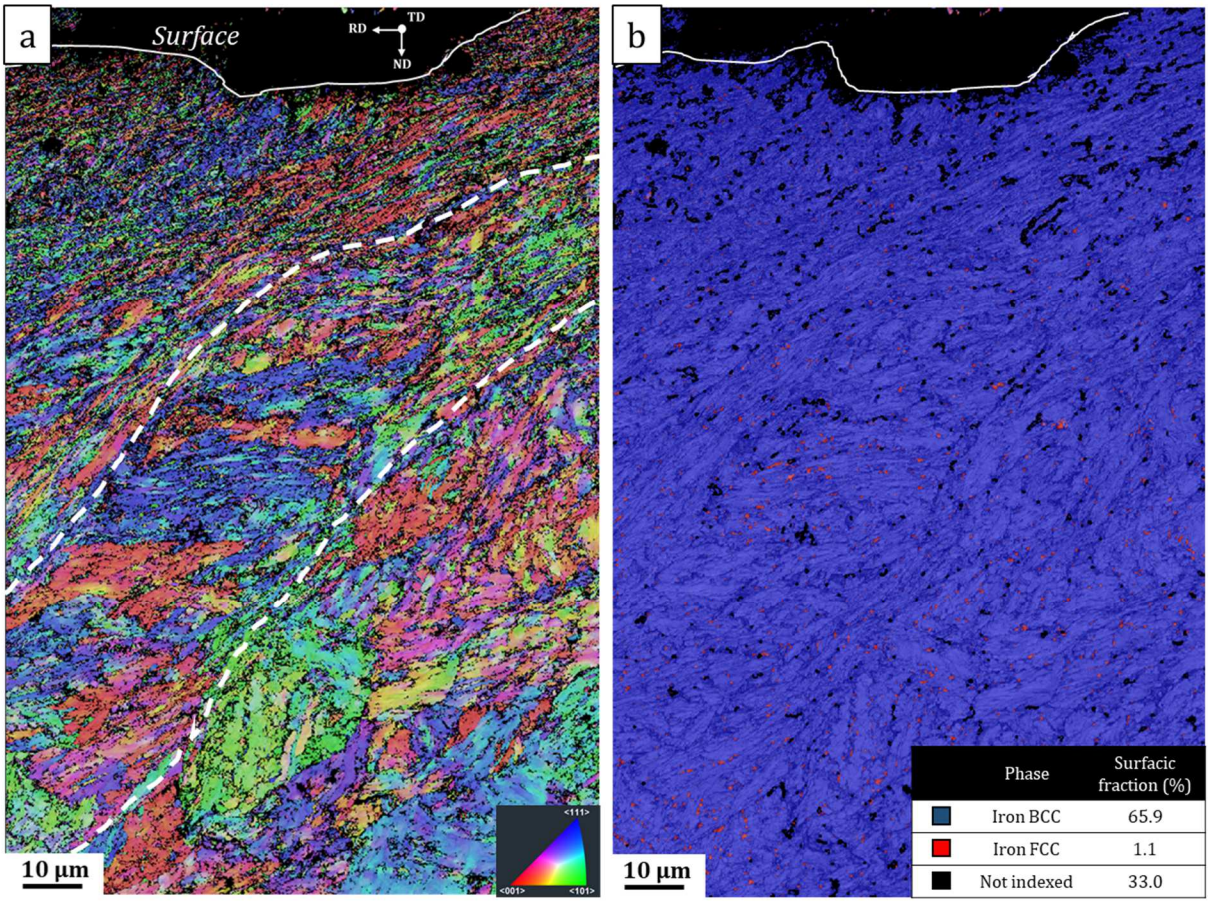

Figure 10: Microstructural evolution in close surface in the base material after rig test: a- orientation mapping following TD. Shear bands are highlighted by dashed line and b- corresponding phases map

These EBSD analyses are completed with Matlab investigations in Figure 11, aiming to quantify the microstructure evolution in close surface. Matlab routine consists in using phase maps obtained by EBSD and consider the 2D global image as a succession of 1D lines of 70 nm width (equal to the scan step size) at different depths. For each depth, a local austenite content (respectively, unindexed pixels content) is measured and averaged with the surrounding two 1D lines. Then, this averaged austenite or unindexed pixel content is plotted as a function of depth.

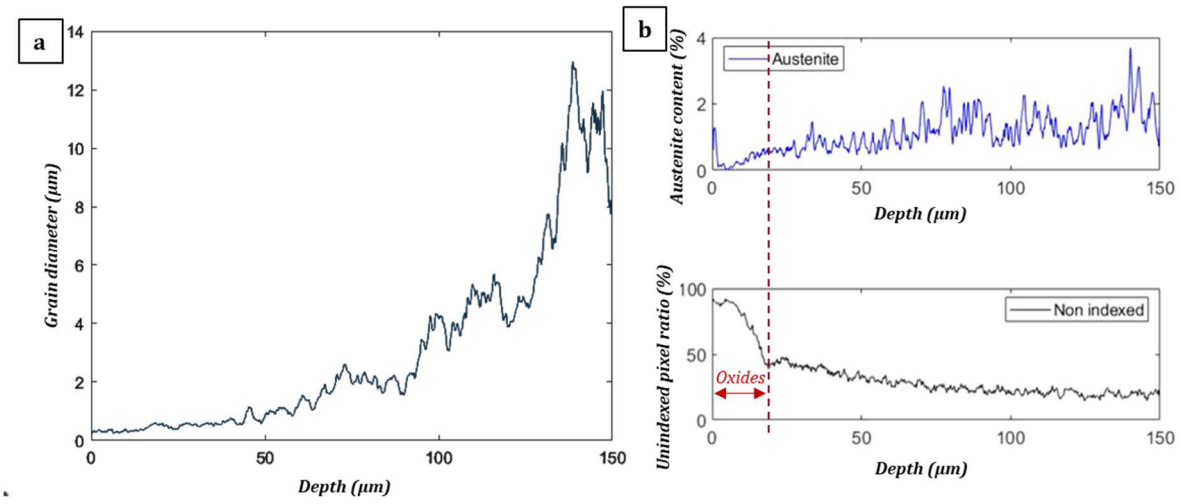

Figure 11 : After rig test: a- Prior austenite grain size evolution along ND in the base material b- Austenite surface content and non-indexed pixels content evolution in close surface in the base material. Analyses made by Matlab.

Figure 10 shows a shearing of the microstructure (highlighted in dashed lines). This shearing is at first close to 0° in the first 20 microns below the surface, then get closer to 45° from 20 micrometers to 100 micrometers below the surface. A microstructure refinement is also observed from the core of the rail to its surface (Figure 11.a), with the formations of sub-micrometrics deformed grains in close surface. Along with this refinement, a diminution of the austenite content is observed (Figure 11.b). This reduction of austenite content originates from two phenomena. The first one is a diminution of the pixel indexing content in close surface (Figure 11.b), which is a consequence of the severe lattice deformation due to wheel-rail contact. The second is the partial transformation from austenite into martensite, following TRansformation Induced Plasticity (TRIP) effect. This TRIP effect will be discussed in detail in section 4.

Thin foils have been sampled at the core of the undeformed rail and at a depth of 70 µm from the rail surface after rig test to compare at a lower scale the microstructure evolution of B320 prior and after rig test. These thin foils have been used for both Transmission Diffraction Kikuchi (TKD) (Figure 12) and Transmission Electron Microscopy (TEM). Around 0.9% untransformed blocky austenite is still observed in the microstructure of the deformed specimen at this depth.

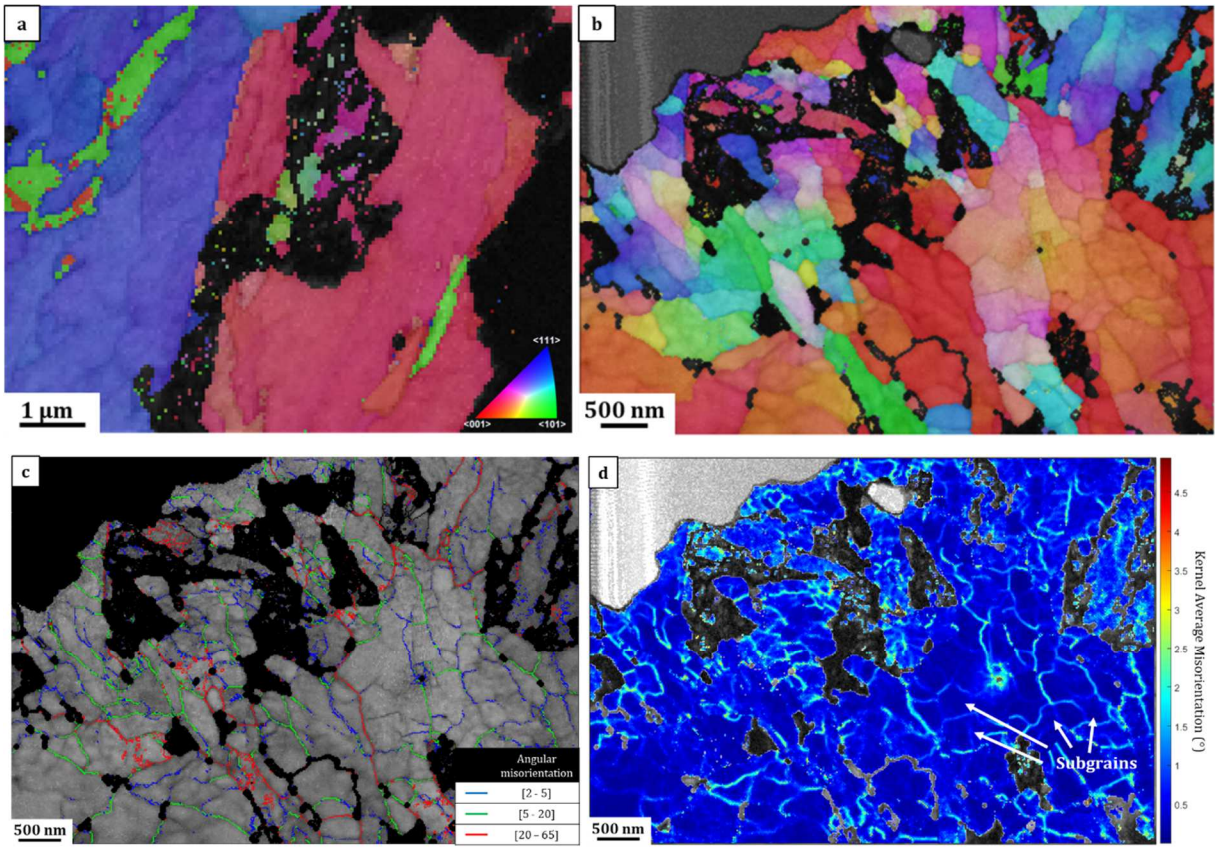

Figure 12: Observations of base material microstructure with TKD investigations following RD showing a- the untested sample microstructure and b- the microstructure at a 70 µm depth from the surface after rig test. c- Misorientations map corresponding to picture b and d- KAM map considering 2 neighbors between 0° and 5° corresponding to picture b. Some sub-grains formed are highlighted by white arrows

Figure 12 clearly confirms the microstructure refinement, with bainitic sheaves refined into sub-micrometric deformed sheaves of around 500 nm width. The formation of sub-grains can be observed on the tested sample at a 70 µm depth (Figure 12.b to Figure 12.d), which suggests that the material experienced recovery. There is no evidence of the formation of high angle boundaries indicating recrystallization at this depth and at this scale (Figure 12.c).

These analyses are completed with TEM investigations on the same specimen, within the same thin section (Figure 13).

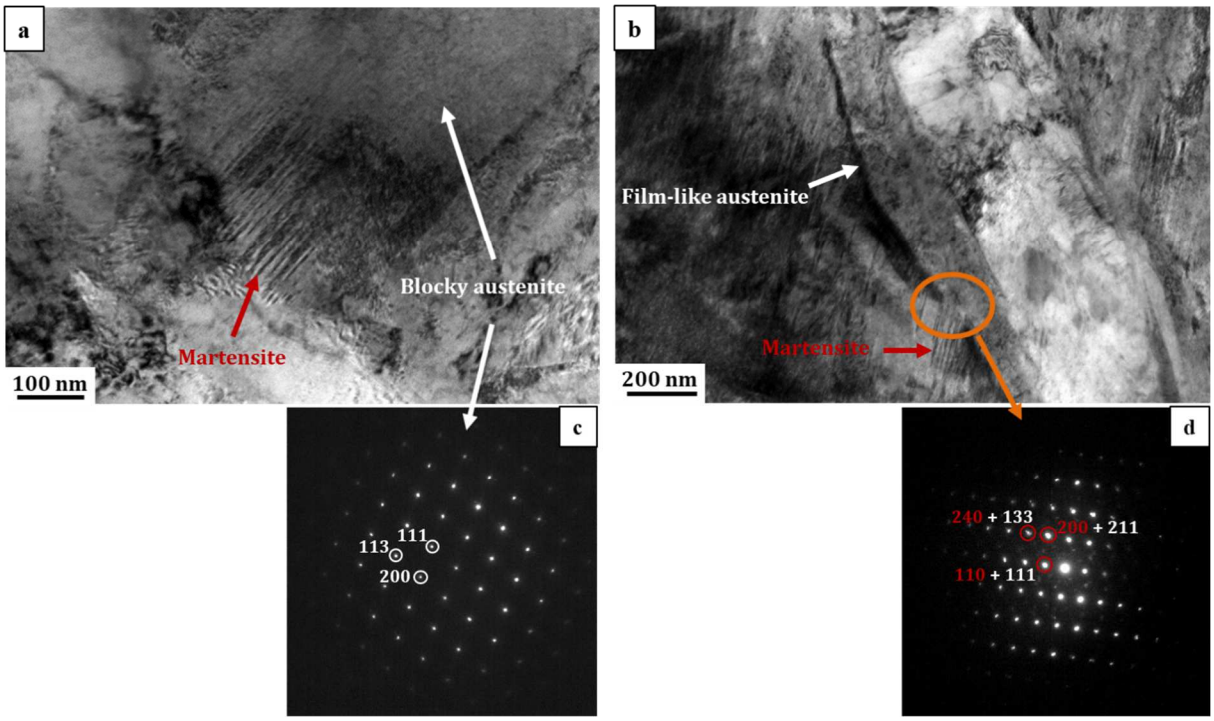

Figure 13: TEM observations of base material microstructure showing the solicitated microstructure at a 70 µm depth. Bright field images a- martensite formed inside austenite block and b- martensite formed along an austenite film. c- corresponds to the diffraction pattern of the blocky austenite presented on image a., following [2 -2 0] zone axis and d- Diffraction pattern of the area highlighted by orange circle. Due to the very small dimensions of the transformed martensite lath, two distinct patterns can be observed: martensite in red (zone axis [0 0 -2]) and austenite in white, slightly distorted from zone axis [0 1 -1]

Figure 13.a and Figure 13.b show the presence of martensite inside the deformed region, along an austenite block as well as an austenite film, respectively. On Figure 13.b, the diffraction patterns of austenite and martensite coexist, which confirm the existence of phase transformation on this zone. These martensitic areas are either formed during rail cooling, or as a result of the TRIP effect occurring inside austenite (blocky and film-like, respectively) after solicitation.

Complementary analyses have been performed with TEM orientation imaging (ASTAR). The existence of film-like austenite has been confirmed by this technique (Figure 14 below). This corresponds to a deformed area, which explains why the observed austenite is of small dimensions compared to the dimensions of the austenite prior to rig test (usually around 100nm wide and 0.5-1µm long).

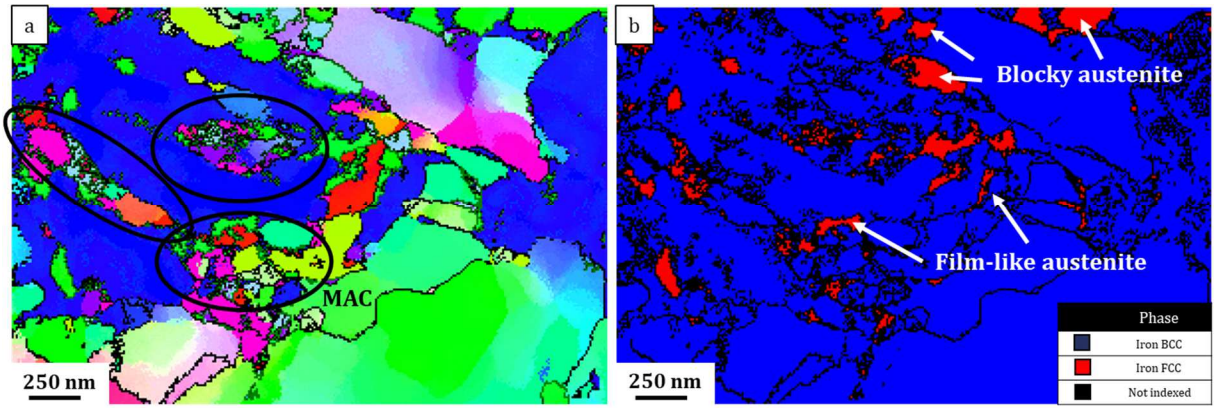

Figure 14 : ASTAR analyses showing a- orientation map and b- phase map of deformed B320 at a 50 µm depth. The presence of austenite at this depth is confirmed by this technique.

On Figure 14, the existence of both film-like austenite and blocky austenite at 50 µm depth is confirmed. However, the dimensions of these films and blocks of austenite are very small in front of the one observed in the unaffected sample, which confirms the microstructure refinement observed previously. MAC fraction is high in front of the one observed in the unaffected material, which is also coherent with the occurrence of TRIP effect.

3.3.2. *Heat Affected Zone (2 cm from the fusion zone)*

As presented earlier, the Heat Affected Zone presents a lower head check resistance compared to the base material, especially at around 2 cm from the fusion zone, where a few microcracks are to be seen (Figure 4). The chemical composition is identical in both base material and HAZ, but the microstructure differs due to the thermal input coming from the welding process, which entails distinct damage mechanisms of these zones during the test rig. The objective of this part is to investigate the differences of microstructure as compared to the base material to identify the parameters impacting HC resistance in bainitic steels.

Figure 15 exhibits the microstructure and phase evolution in close surface for the HAZ at 2 cm from the fusion zone.

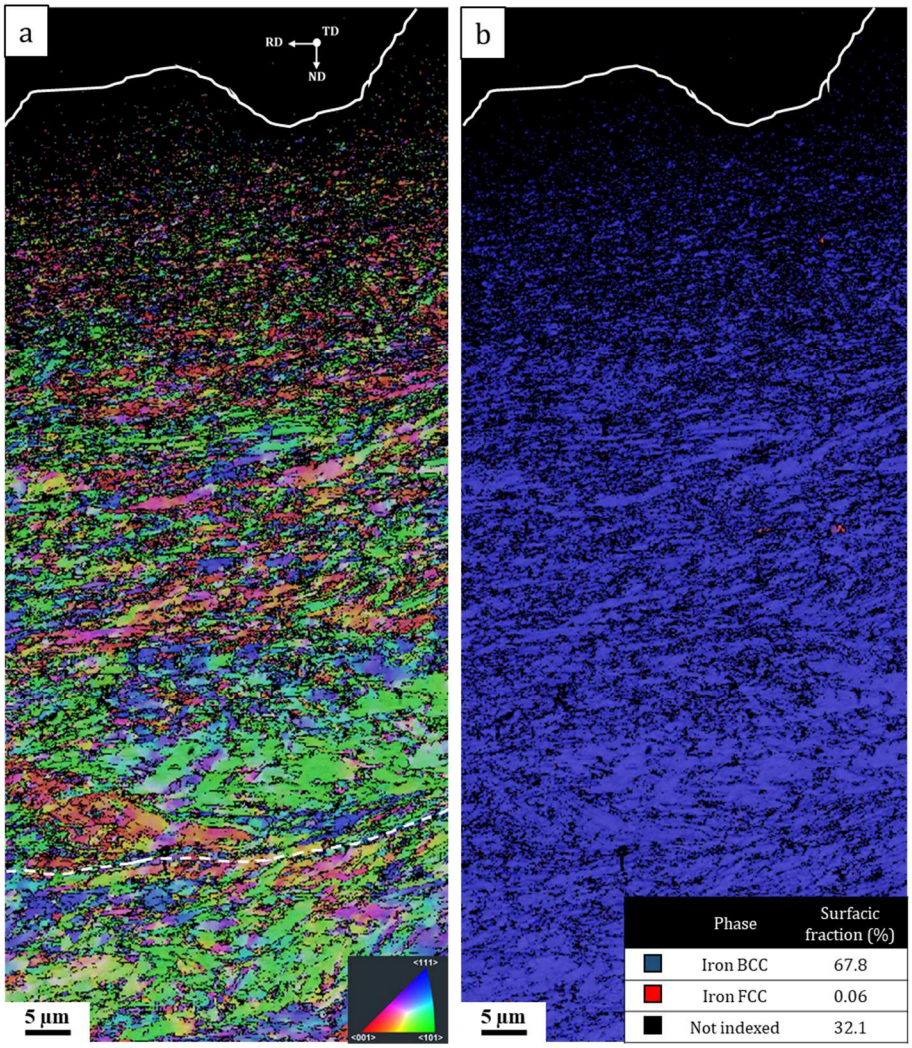

Figure 15: Microstructural evolution in close surface in the Heat Affected Zone at 2 cm from the fusion zone along RD after rig test: a- orientation mapping coupled with band contrast. Dashed line highlighting the shearing of the microstructure and b- corresponding phases map

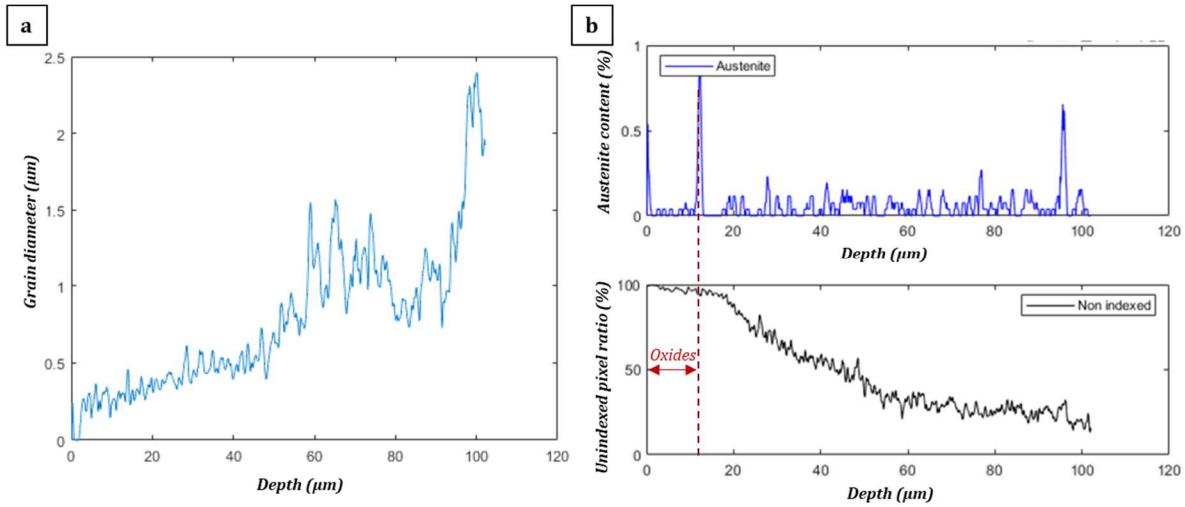

Figure 16: HAZ at 2 cm from FZ along RD after rig test: a- Grain size evolution along ND and b- Austenite content and non-indexed pixels content evolution along ND. Analyses made by Matlab

The shearing of the microstructure, previously observed at around 45° from the rolling direction is, in this case, closer to 0° (parallel to the rolling direction) in several tenths of microns. The microstructure refinement (Figure 16.a) is similar to the one observed in the base material, even if the grain size evolution is not as straightforward as it is in the base material. However, one can notice the almost complete absence of austenitic phase (Figure 16.b) in close surface for this region. Since almost no austenite is found at around 100 µm depth, where the indexing rate is high, the absence of austenite is not believed to originate from indexing failure, but rather corresponds to an actual absence of this phase. The low content of austenite existing prior to rig test (Table 6) is no more observed, which is probably explained by its transformation into martensite. This transformation is then confirmed by low-scale analyses (Figure 17).

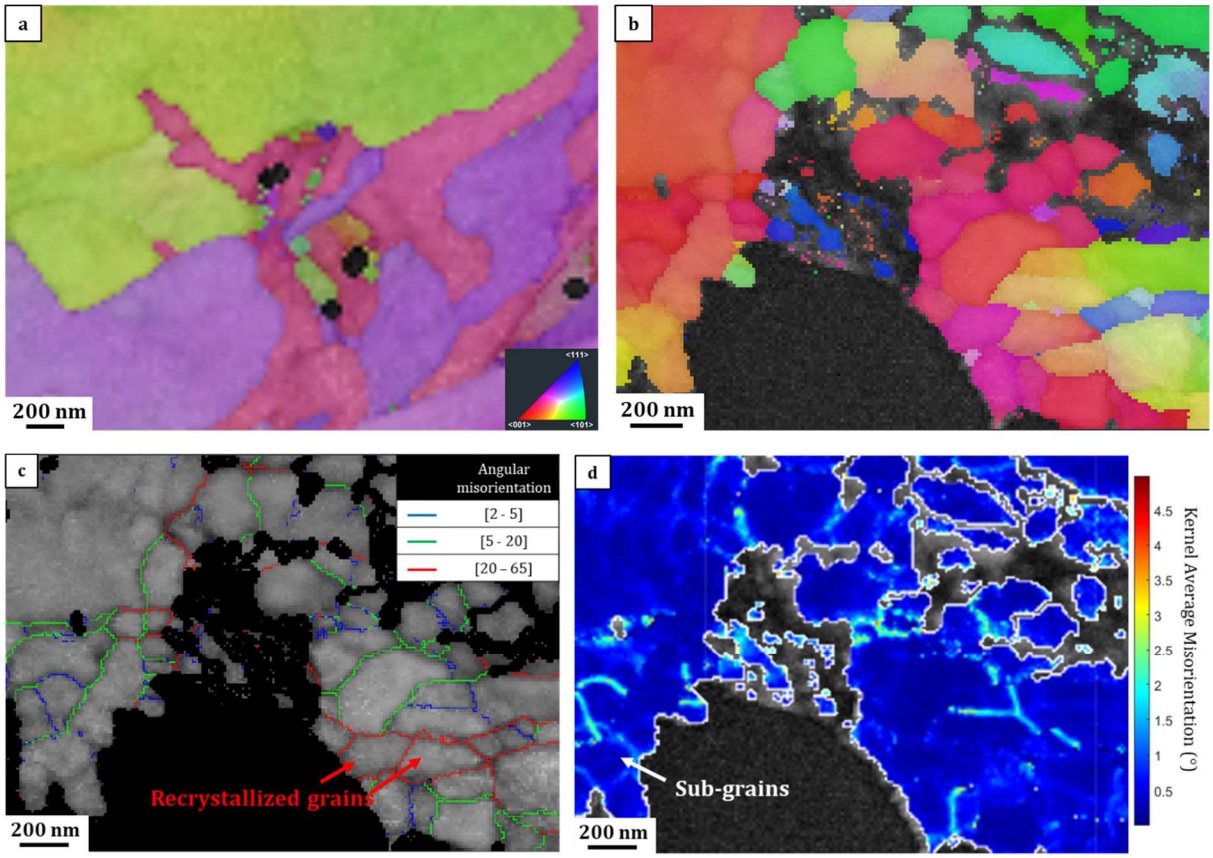

Figure 17: Observations of the microstructure in the HAZ at 2 cm from fusion zone along RD with TKD investigations showing a- the core microstructure and b- the microstructure at a 70 µm depth from the surface after rig test. c- Misorientations map corresponding to picture b) and d- KAM map considering 2 neighbors between 0° and 5° corresponding to picture b. Some sub-grains formed are highlighted by white arrows on Figure 17.d, while probable recrystallized grains are indicated by red arrows on Figure 17.c

As seen earlier, a clear microstructure refinement is confirmed by TKD investigations. The formation of sub-micrometric grains of diameter close to 250 nm is confirmed at a 70 µm depth. The retained austenite content measured by EBSD is null in this region (Table 7), while almost 1% austenite remained at the same depth inside base material. Compared to base material, some high angle grain boundaries, likely to correspond to recrystallization are observed (Figure 17.c). Conversely, recovery and sub-grains formation (Figure 17.d) are less pronounced compared to base material.

TEM analyses are then performed on this thin section (Figure 18). Martensite is observed between austenitic films and blocks, similarly to what was previously seen in the base material.

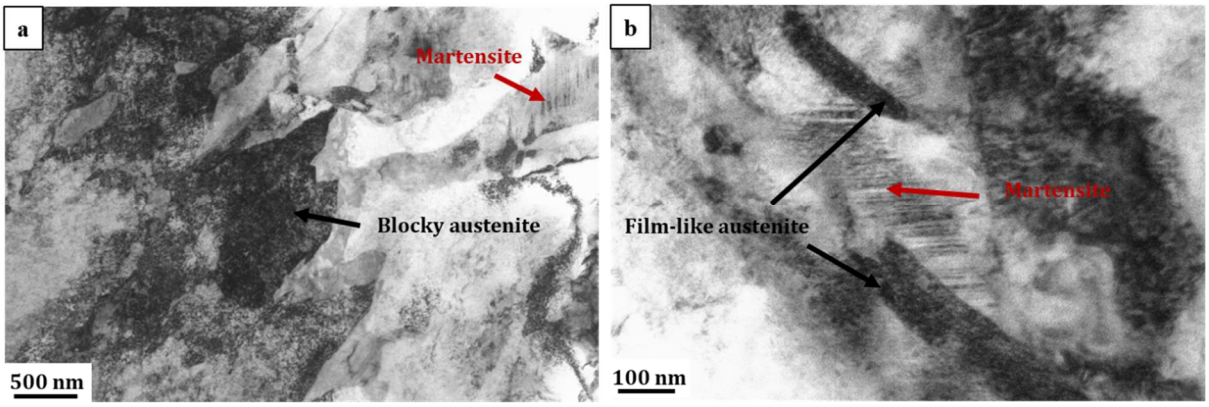

Figure 18: Microstructure of the heat affected zone observed at a depth of 70 µm from the surface showing a- martensite as well as blocky austenite and b- martensite formed among a film-like austenite. Diffraction pattern of martensite is indicated on the top part of the image

Table 7 presents a summary of the investigations performed on the tested samples at a depth of 70 µm.

Table 7: Summary of the microstructural features observed in the tested specimens at a 70µm depth in both base material and HAZ at 2 cm from the FZ along the rolling direction.

	Base material	HAZ 2cm
Grain size (nm)	500 *± 100*	250 *± 100*
Presence of martensite	Yes	Yes
Untransformed retained austenite (%)	0.9%	< 0.05%
Unindexed pixel content (%)	~ 35%	~ 30%
Main phenomena observed	Shearing Recovery Recrystallization	Shearing Recovery Recrystallization

As seen in this table, the microstructure refinement is more pronounced in the HAZ compared to the base material, with a lower grain size observed in the HAZ. Both microstructures experienced TRIP effect, with martensite observed among film-like austenite and blocky austenite. However, the amount of austenite remaining at the end of rig test is significantly lower in the HAZ, with no untransformed retained austenite measured at 70 µm depth, while a few (0.9%) retained austenite is still measured in the base material at the same depth.

4. Discussion

The excellent HC resistance has been observed for the B320 bainitic steel grade (Figure 4). R260 pearlitic steel tested under identical solicitation presented a crack network, while very few micro-cracks along the sub surface could be observed in B320 CFB steel grade. However, the wear resistance is significantly lower in the B320 steel grade compared to the classical R260 steel (Figure 3).

While overall head check resistance is outstanding in B320, the Heat Affected Zone corresponds to a critical region, where a few cracks could be observed. These cracks are mostly observed at 2 cm from the fusion zone along the rolling direction, indicating a lower head check resistance in this specific area.

To identify the origins of these microcracks, the initial microstructural (Table 5) and solicitated microstructure (Table 7) of both base material and HAZ of B320 grade have been compared. One of the key parameters identified regarding the initial microstructure is the phases contents, which have been presented in Table 5 and summed up in Figure 19.

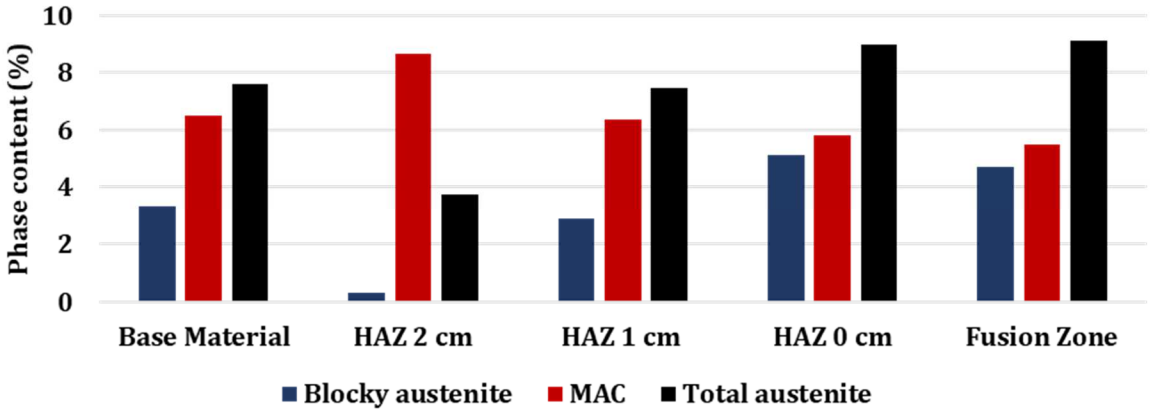

Figure 19: Initial blocky austenite, MAC and total austenite contents before rig test for different rail localizations

The HAZ at 2 cm from the FZ along the rolling direction presents singular phases contents compared to the remaining part of the rail (Figure 19). The MAC content is the highest, while the austenite content is the lowest in this region. More specifically, the blocky austenite content is almost null, while several percent of blocky austenite are found in the remaining part of the rail. The low initial amount of austenite in this region is a consequence of the thermal input induced by the welding process, leading to its transformation. While it is hard to assess the exact phenomenon occurring without having knowledge of the local thermal history, it is believed that close to the fusion zone (CGHAZ), the temperature is high compared to Ac3, leading to austenitizing during welding. Therefore, inside CGHAZ, supplementary austenite is produced during heating while a few martensite is formed during cooling. However, when getting far from the FZ, the peak temperature experienced by the material gets lower and lower, until it gets intermediary between Ac1 and Ac3 (ICHAZ). In this area, less austenite is produced due to rail heating after welding but some of the preexisting austenite might be thermally transformed into martensite, which would result in a diminution of the global austenite content and an increase of the MAC content. This corresponds to the microstructure observed at 2 cm from the FZ. A better knowledge of the accurate thermal history of the HAZ would confirm these post-mortem observations.

Once microcracks are formed after rig test, their propagation is of primordial importance. In B320 CFB rail, these microcracks are believed to propagate slowly due to the combined role of film-like

austenite and TRIP effect, as discussed previously. The presence of martensite has been confirmed in every region of the rail (Table 7). Moreover, while the base material still presents a few untransformed austenite at a 70 µm depth (0.9% measured by EBSD), almost no untransformed austenite remains in the HAZ at the same depth (<< 0.1%). This indicates that TRIP effect can no longer occur in blocky austenite in the HAZ at this depth, since it has already been fully transformed. The positive TRIP effect has therefore disappeared inside the HAZ and replaced by the detrimental contribution of the martensite. Thus, the head check resistance of the HAZ is lower compared to the base material.
However, while HC resistance is high in B320 CFB, the wear rate is high, leading to material wear off in extreme surface. Surface loss is high in front of the microcracks length and depth, which might lead to the hindering of previously formed HC microcracks.

The role of both retained austenite (RA) and martensite is discussed. The effect of RA on HC resistance is controversial in the literature and varies according to its shape.
Film-like austenite improves the strength and toughness of the bainitic steel [40]. It also lowers crack propagation rate by adding austenite-bainitic ferrite interfaces that are highly energy consuming to cross [36]. Lowering the distance between austenite films leads to an increase of the amount of barriers to be crossed by cracks during their propagation, which is beneficial to both wear and HC resistance [3,38]. Grades containing film-like RA such as B320 do not exhibit head check or spalling, compared to those containing only blocky RA [57].
Blocky austenite is considered to be detrimental to the mechanical properties [30], with the noticeable exception of ductility increase [28]. Blocky RA is known to be prone to crack nucleation and eases crack propagation [58]. However, while the mechanical stability of film-like RA was shown to be high due to its relatively high carbon content [10,35,59,60], blocky RA is more prone to TRansformation Induced Plasticity (TRIP) effect [39,58]. Shen *et al.* [61] for example measured, in a 0.19 wt% C TRIP-assisted multi-phase steel, a carbon content ranging from 0.8 wt% C to 1.1 wt% C inside film-like RA while carbon content in blocky RA was closer to 0.6 wt% C.
The transformation from austenite into martensite induces an increase in sub-surface hardness [13] and work hardening capacity [28]. Moreover, the transformation process itself induces a compressive stress in the surroundings, due to the crystal volume expansion generated by martensitic transformation [60,62]. That compressive stress delays microvoid formation around RA, which plays a vital role in enhancing the total elongation of bainitic steels [32,63,64]. This compressive stress also reduces crack propagation speed and induces crack tip closure. Furthermore, this transformation consumes energy resulting from mechanical straining, hereby reducing the available energy for fatigue crack growth [33,65]. Crack growth rate is lowered, and head check resistance is increased. Due to TRIP effect and the lowering of crack propagation rate, most studies agree that a high content of RA is beneficial for HC resistance [28] and crack propagation resistance [66,67].

, a too high RA content leads to massive amount of transformed martensite *via* TRIP effect. Martensite is believed to be detrimental to HC resistance due to the formation of cracks at the bainitic ferrite-martensite interface originating from large strain incompatibility [25]. Moreover, the brittle nature [40,68] of martensite makes it a preferential crack propagation path, hereby increasing the crack propagation rate. This is confirmed experimentally (Figure 20), with a few micro-cracks observed after rig test inside or around martensitic phase. The cracks can either grow through the MAC (Figure 20.a) or at the interface between MAC and surrounding bainitic ferrite (Figure 20.b).

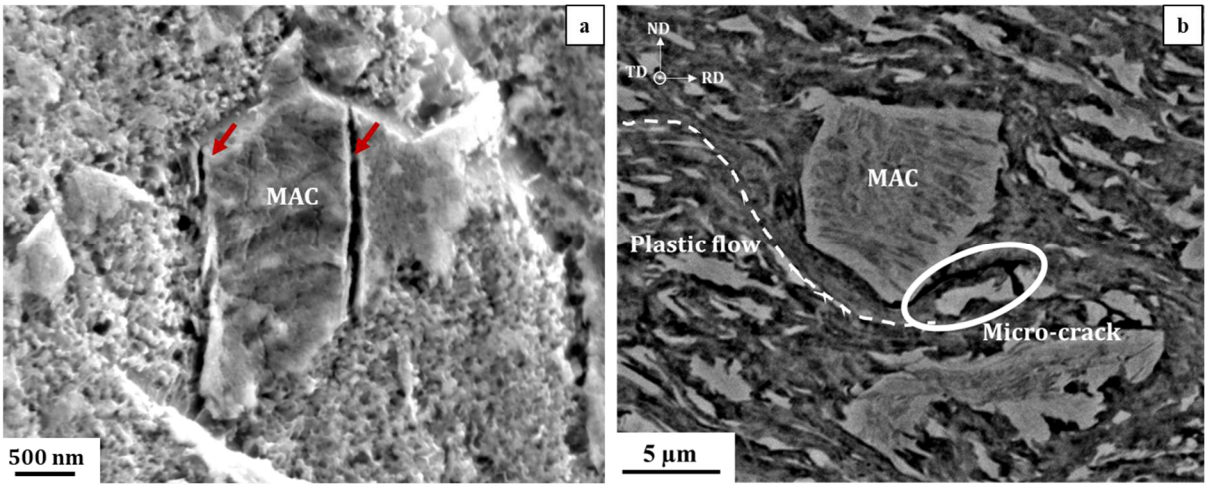

Figure 20: Cracks observed a- through a MAC and b- at the interface between a MAC and surrounding bainitic ferrite

As a result, an optimum distribution between blocky austenite (enhanced TRIP effect) and film-like austenite (lowering crack propagation and delayed TRIP effect) is to be found to optimize head check resistance.

The present microstructural observations lead to the proposal of a degradation mechanism in the B320 steel grade during rail solicitation. This mechanism is then split depending on the considered rail position: either in the base material (Figure 21) or in the HAZ (Figure 22).

The degradation mechanism in the base material can be summed up in four stages (Figure 21):

- **Stage I:** In the early stage of the solicitation, the initial microstructure composed of blocky austenite, film-like austenite and a few martensite-austenite compounds is slightly deformed. The TRIP effect occurs rapidly, especially inside the blocky RA, whose stability is lower. The phase transformation occurs preferentially in close surface, where the mechanical solicitation is the highest. This TRIP effect will still be effective as long as sufficient RA (blocky and/or film-like) is available.
- **Stage II:** Cracks are initiated, mainly at interfaces between bainitic ferrite and martensite or inclusion (*e.g.* MnS). Shearing leads to cracking in close surface when the local solicitation gets high enough.
- **Stage III:** Crack propagates along the subsurface of the rail. Due to the energy consumption and compressive force induced by TRIP effect, the crack propagation speed is low. The RA films also lower crack propagation speed, leading to an overall hardly propagating crack. RA in close surface

is believed to be partly transformed into martensite at this point, but a small proportion remains at a 70 µm depth (Table 7) after rig test. This presence of blocky austenite remaining at this depth indicates that TRIP is still in process and crack propagation is still slowed down.

- **Stage IV:** Simultaneously to crack propagation, abrasive wear occurs. The low wear resistance of B320 bainitic steel implies a high wear rate. This wear leads to material wear off in extreme surface, hereby hindering previously formed cracks. Abrasive wear leads to the suppression of the extreme surface which leads to the surfacing of a deeper microstructure. This "refreshed" microstructure is only slightly affected by rolling contact fatigue at this point, which means that its martensite content is still relatively low. TRIP effect can therefore be prolongated in further solicitation. Abrasive wear rate is probably higher than the crack propagation speed, which would explain that no crack is observed in worn material. Thus, the rail is worn but the microstructure is free of head check defects.

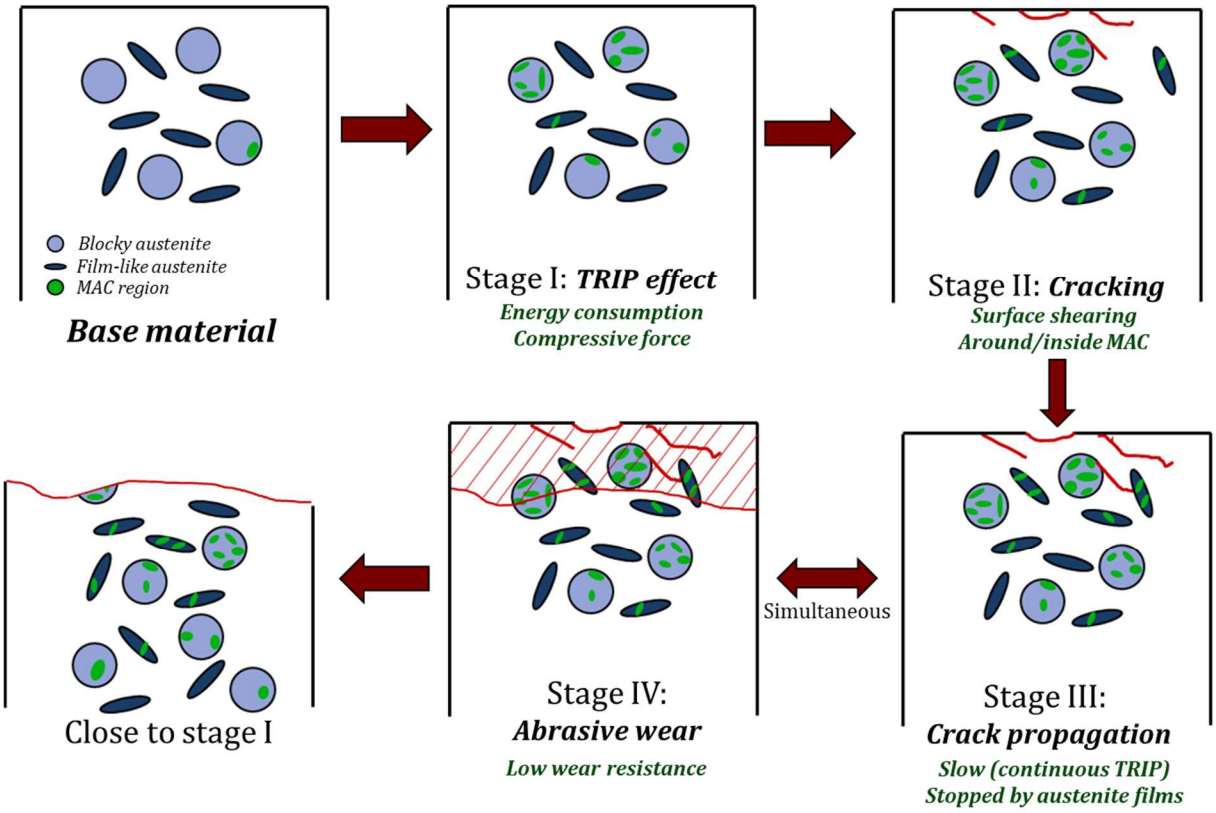

Figure 21: degradation mechanisms in the base material of B320 bainitic steel grade.

In the ICHAZ, the initial blocky RA content is very low while the MAC content is high compared to the base material. This indicates that a lower amount of austenite is available for martensitic transformation, which would lead in a severely shortened TRIP effect (Stage I). Moreover, the increased content of MAC might induce more crack initiation sites during Stage II. When reaching Stage III, most of the blocky austenite has already been transformed (Table 7), which increases crack propagation rate due to the termination of TRIP effect. Abrasive wear (Stage IV) is almost identical to what is observed in the base material, with only a slight increase of wear rate measured

macroscopically. In the end, the wear rate is closer to the crack propagation speed, which leads to the emergence of a few cracks in the sub-surface. This altered mechanism adapted to HAZ conditions is summed up in Figure 22.

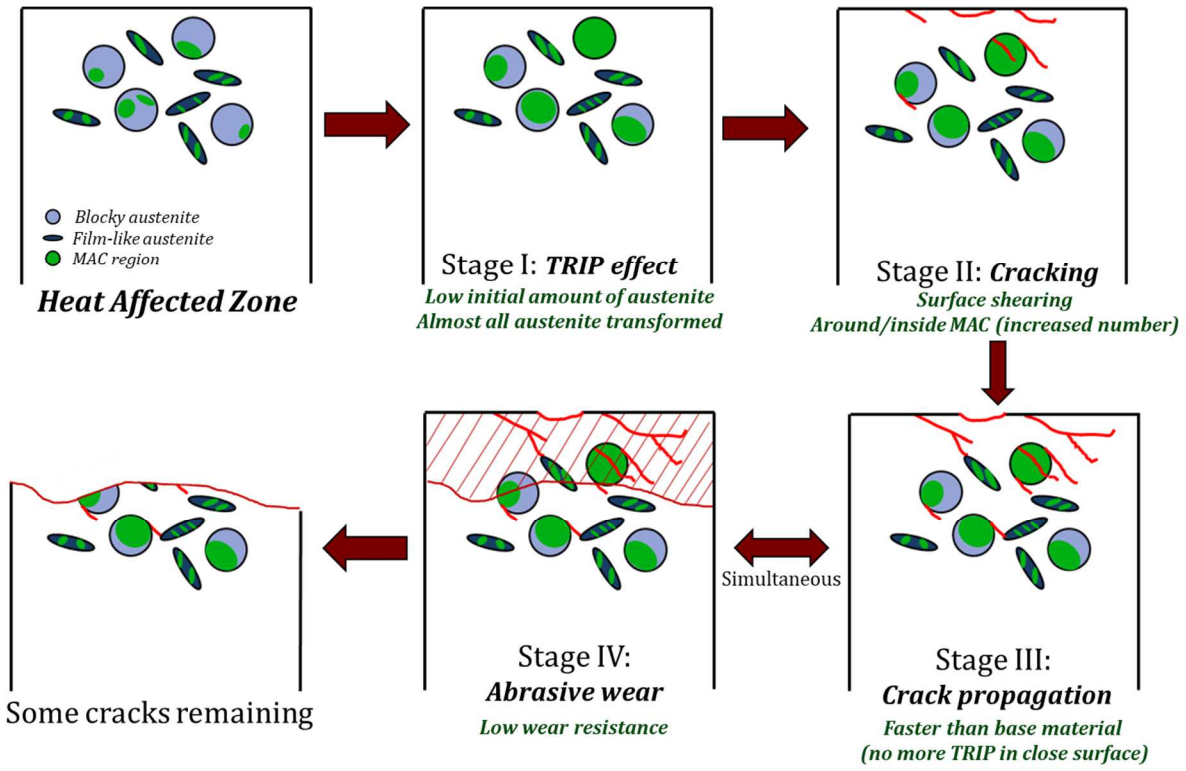

Figure 22: Degradation mechanism in the HAZ of B320 bainitic steel grade at 2 cm from the Fusion Zone along the rolling direction.

5. *Conclusions*

The Head Check (HC) resistance of a B320 bainitic steel rail has been investigated after laboratory testing at the Deutsche Bahn's rig test A and compared to classical R260 pearlitic steel.

Both R260 and B320 present their own advantages. R260 shows high wear resistance and is therefore perfectly suited in places where head check does not occur *i.e.* in straight lines. However, its low HC resistance make it less performant in switches, crossings, or more generally in curves. Conversely, B320 presents a low wear resistance compared to R260 in these conditions, but extremely high HC resistance, making it a perfect candidate for switches and crossings.

While no crack could be observed inside the base material and the fusion zone, a few microcracks could be detected in the Heat Affected Zone (HAZ) at a distance of 2 cm from the fusion zone along the rolling direction. Thus, the microstructure of B320 base material has been compared with the microstructure of the HAZ at the aforesaid position in order to determine the differences existing between these two areas. The main microstructural difference between base material and HAZ is their phases contents. The HAZ presents a low retained austenite content going with a high Martensite-Austenite Compound (MAC) content. A degradation mechanism for B320 carbide free rail is then proposed in 4 steps, namely:

1- Transformation from retained austenite into martensite, following TRIP effect.

2- Crack initiation mostly at the surface and inside or in the vicinity of MAC.

3- Crack propagation whose speed is slow due to the existence of film-like austenite and TRIP effect.

4- Abrasive wear.

Steps 3 and 4 compete and occur simultaneously. The resulting rail defects (wear, fatigue…) depend on the competition between wear rate and crack propagation speed. Inside the base material, the combined effect of film-like austenite and TRIP effect leads to a very slow crack propagation rate. Conversely, inside the HAZ, the retained austenite content is low, and becomes almost null at a depth of 70 µm after rig test. This indicates that the initial austenite content was not high enough in this region to ensure a continuous TRIP effect. Thus, crack propagation rate is increased, and a few cracks emerge at the close surface.

Acknowledgments

This project has received funding from the European Union's Horizon 2020 research and innovation program under grant agreement No:826255 (IN2TRACK2).

The SEM and TEM national facilities in Lille (France) are supported by the Conseil Régional du Nord-Pas de Calais, the European Regional Development Fund (ERDF), and the Institut National des Sciences de l'Univers (INSU, CNRS).

The authors would also like to thank P. Roussel (Université de Lille, France) for XRD experiments, Goldshmidt (Rainham, United Kingdom) for thermit welding, Saarstahl Rail (Hayange, France) for rail producing and Deutsche Bahn (Kirchmöser, Germany) for rig test performed.

References

[1] A. Ekberg, E. Kabo, Fatigue of railway wheels and rails under rolling contact and thermal loading—an overview, Wear. 258 (2005) 1288–1300. https://doi.org/10.1016/j.wear.2004.03.039.

[2] Q. Li, X. Huang, W. Huang, Fatigue property and microstructure deformation behavior of multiphase microstructure in a medium-carbon bainite steel under rolling contact condition, Int. J. Fatigue. 125 (2019) 381–393. https://doi.org/10.1016/j.ijfatigue.2019.04.019.

[3] S. Hasan, Dry rolling/sliding wear behaviour of pearlitic rail and newly developed carbide-free bainitic rail steels, Wear. (2018) 9.

[4] C.C. Viáfara, M.I. Castro, J.M. Vélez, A. Toro, Unlubricated sliding wear of pearlitic and bainitic steels, Wear. 259 (2005) 405–411. https://doi.org/10.1016/j.wear.2005.02.013.

[5] R.P. Dollevoet, Design of an anti head check profile based on stress relief, University of Twentee, 2010.

[6] M. Steenbergen, R. Dollevoet, On the mechanism of squat formation on train rails – Part I: Origination, Int. J. Fatigue. 47 (2013) 361–372. https://doi.org/10.1016/j.ijfatigue.2012.04.023.

[7] Y. Chen, R. Ren, J. Pan, R. Pan, X. Zhao, Microstructure evolution of rail steels under different dry sliding conditions: A comparison between pearlitic and bainitic microstructures, Wear. 438–439 (2019) 203011. https://doi.org/10.1016/j.wear.2019.203011.

[8] H. Chen, Y. Ji, C. Zhang, W. Liu, H. Chen, Z. Yang, L.-Q. Chen, L. Chen, Understanding cementite dissolution in pearlitic steels subjected to rolling-sliding contact loading: A combined experimental and theoretical study, Acta Mater. 141 (2017) 193–205. https://doi.org/10.1016/j.actamat.2017.09.017.

[9] X. Sauvage, J. Copreaux, F. Danoix, D. Blavette, Atomic-scale observation and modelling of cementite dissolution in heavily deformed pearlitic steels, Philos. Mag. A. 80 (2000) 781–796. https://doi.org/10.1080/01418610008212082.
[10] H.K.D.H. Bhadeshia, Bainite in steels: theory and practice, Third edition, Maney Publishing, Leeds, UK, 2015.
[11] F. Manieri, K. Stadler, G.E. Morales-Espejel, A. Kadiric, The origins of white etching cracks and their significance to rolling bearing failures, Int. J. Fatigue. 120 (2019) 107–133. https://doi.org/10.1016/j.ijfatigue.2018.10.023.
[12] H.W. Zhang, S. Ohsaki, S. Mitao, M. Ohnuma, K. Hono, Microstructural investigation of white etching layer on pearlite steel rail, Mater. Sci. Eng. A. 421 (2006) 191–199. https://doi.org/10.1016/j.msea.2006.01.033.
[13] A. Kumar, A.K. Saxena, C. Kirchlechner, M. Herbig, S. Brinckmann, R.H. Petrov, J. Sietsma, In situ study on fracture behaviour of white etching layers formed on rails, Acta Mater. 180 (2019) 60–72. https://doi.org/10.1016/j.actamat.2019.08.060.
[14] J. Wen, J. Marteau, S. Bouvier, M. Risbet, F. Cristofari, P. Secordel, Comparison of microstructure changes induced in two pearlitic rail steels subjected to a full-scale wheel/rail contact rig test, Wear. 456–457 (2020) 203354. https://doi.org/10.1016/j.wear.2020.203354.
[15] A.M. Elwazri, P. Wanjara, S. Yue, The effect of microstructural characteristics of pearlite on the mechanical properties of hypereutectoid steel, Mater. Sci. Eng. A. 404 (2005) 91–98. https://doi.org/10.1016/j.msea.2005.05.051.
[16] P. Clayton, D. Danks, Effect of interlamellar spacing on the wear resistance of eutectoid steels under rolling-sliding conditions, Wear. 135 (1990) 369–389. https://doi.org/10.1016/0043-1648(90)90037-B.
[17] M. das G.M. da Fonseca Gomes, L.H. de Almeida, L.C.F.C. Gomes, I. Le May, Effects of microstructural parameters on the mechanical properties of eutectoid rail steels, Mater. Charact. 39 (1997) 1–14. https://doi.org/10.1016/S1044-5803(97)00086-7.
[18] K. Sawley, Rolling Contact Fatigue: a comprehensive review, Federal Railroad Administration, Washington DC, 2011.
[19] X.Y. Feng, F.C. Zhang, J. Kang, Z.N. Yang, X.Y. Long, Sliding wear and low cycle fatigue properties of new carbide free bainitic rail steel, Mater. Sci. Technol. 30 (2014) 1410–1418. https://doi.org/10.1179/1743284713Y.0000000474.
[20] K. Wang, Z. Tan, C. Cheng, B. Gao, G. Gao, R.D.K. Misra, B. Bai, Effect of microstructure on the spalling damage in a 20Mn2SiCrMo bainitic rail, Eng. Fail. Anal. 70 (2016) 343–350. https://doi.org/10.1016/j.engfailanal.2016.09.011.
[21] J. Debehets, J. Tacq, A. Favache, P. Jacques, J.W. Seo, B. Verlinden, M. Seefeldt, Analysis of the variation in nanohardness of pearlitic steel: Influence of the interplay between ferrite crystal orientation and cementite morphology, Mater. Sci. Eng. A. 616 (2014) 99–106. https://doi.org/10.1016/j.msea.2014.08.019.
[22] H. Yokoyama, S. Mitao, S. Yamamoto, Y. Kataoka, T. Sugiyama, High Strength Bainitic Steel Rails for Heavy Haul Railways with Superior Damage Resistance, (2001) 8.
[23] A.M. Gola, M. Ghadamgahi, S.W. Ooi, Microstructure evolution of carbide-free bainitic steels under abrasive wear conditions, Wear. 376–377 (2017) 975–982. https://doi.org/10.1016/j.wear.2016.12.038.
[24] C. Garcia-Mateo, F.G. Caballero, M.K. Miller, J.A. Jimenez, On measurement of carbon content in retained austenite in a nanostructured bainitic steel, J. Mater. Sci. 47 (2012) 1004–1010. https://doi.org/10.1007/s10853-011-5880-2.
[25] S.M. Hasan, A. Mandal, S.B. Singh, D. Chakrabarti, Work hardening behaviour and damage mechanisms in carbide-free bainitic steel during uni-axial tensile deformation, Mater. Sci. Eng. A. 751 (2019) 142–153. https://doi.org/10.1016/j.msea.2019.02.062.
[26] Y.F. Shen, L.N. Qiu, X. Sun, L. Zuo, P.K. Liaw, D. Raabe, Effects of retained austenite volume fraction, morphology, and carbon content on strength and ductility of nanostructured TRIP-assisted steels, Mater. Sci. Eng. A. 636 (2015) 551–564. https://doi.org/10.1016/j.msea.2015.04.030.

[27] A.S. Podder, I. Lonardelli, A. Molinari, H.K.D.H. Bhadeshia, Thermal stability of retained austenite in bainitic steel: an in situ study, Proc. R. Soc. Math. Phys. Eng. Sci. 467 (2011) 3141–3156. https://doi.org/10.1098/rspa.2011.0212.
[28] P.V. Moghaddam, J. Hardell, E. Vuorinen, B. Prakash, The role of retained austenite in dry rolling/sliding wear of nanostructured carbide-free bainitic steels, Wear. 428–429 (2019) 193–204. https://doi.org/10.1016/j.wear.2019.03.012.
[29] H.K.D.H. Bhadeshia, D.V. Edmonds, Bainite in silicon steels: new composition–property approach Part 2, Met. Sci. 17 (1983) 420–425. https://doi.org/10.1179/030634583790420646.
[30] H.L. Yi, K.Y. Lee, H.K.D.H. Bhadeshia, Mechanical stabilisation of retained austenite in δ-TRIP steel, Mater. Sci. Eng. A. 528 (2011) 5900–5903. https://doi.org/10.1016/j.msea.2011.03.111.
[31] K.-I. Sugimoto, M. Kobayashi, S.-I. Hashimoto, Ductility and strain-induced transformation in a high-strength transformation-induced plasticity-aided dual-phase steel, Metall. Trans. A. 23 (1992) 3085–3091. https://doi.org/10.1007/BF02646127.
[32] P. Jacques, Q. Furnémont, T. Pardoen, F. Delannay, On the role of martensitic transformation on damage and cracking resistance in TRIP-assisted multiphase steels, Acta Mater. 49 (2001) 139–152. https://doi.org/10.1016/S1359-6454(00)00215-9.
[33] S.D. Antolovich, B. Singh, On the toughness increment associated with the austenite to martensite phase transformation in TRIP steels, Metall. Mater. Trans. B. 2 (1971) 2135–2141. https://doi.org/10.1007/BF02917542.
[34] L.C. Chang, The rolling/sliding wear performance of high silicon carbide-free bainitic steels, Wear. 258 (2005) 730–743. https://doi.org/10.1016/j.wear.2004.09.064.
[35] Z.N. Yang, Y.L. Ji, F.C. Zhang, M. Zhang, B. Nawaz, C.L. Zheng, Microstructural evolution and performance change of a carburized nanostructured bainitic bearing steel during rolling contact fatigue process, Mater. Sci. Eng. A. 725 (2018) 98–107. https://doi.org/10.1016/j.msea.2018.04.015.
[36] X.Y. Long, J. Kang, B. Lv, F.C. Zhang, Carbide-free bainite in medium carbon steel, Mater. Des. 64 (2014) 237–245. https://doi.org/10.1016/j.matdes.2014.07.055.
[37] G. Gao, K. Wang, H. Su, X. Gui, Z. Li, R.D.K. Misra, B. Bai, The potential of mechanical twinning in ultrafine retained austenite to enhance high cycle fatigue property of advanced bainitic steels, Int. J. Fatigue. 139 (2020) 105804. https://doi.org/10.1016/j.ijfatigue.2020.105804.
[38] W.J. Salesky, G. Thomas, Medium carbon steel alloy design for wear applications, Wear. 75 (1982) 21–40. https://doi.org/10.1016/0043-1648(82)90138-7.
[39] G. Gao, R. Liu, K. Wang, X. Gui, R.D.K. Misra, B. Bai, Role of retained austenite with different morphologies on sub-surface fatigue crack initiation in advanced bainitic steels, Scr. Mater. 184 (2020) 12–18. https://doi.org/10.1016/j.scriptamat.2020.03.036.
[40] G. Gao, B. Zhang, C. Cheng, P. Zhao, H. Zhang, B. Bai, Very high cycle fatigue behaviors of bainite/martensite multiphase steel treated by quenching-partitioning-tempering process, Int. J. Fatigue. 92 (2016) 203–210. https://doi.org/10.1016/j.ijfatigue.2016.06.025.
[41] G. Lacroix, T. Pardoen, P.J. Jacques, The fracture toughness of TRIP-assisted multiphase steels, Acta Mater. 56 (2008) 3900–3913. https://doi.org/10.1016/j.actamat.2008.04.035.
[42] H.K.D.H. Bhadeshia, Some phase transformations in steels, Mater. Sci. Technol. 15 (1999) 22–29. https://doi.org/10.1179/026708399773002773.
[43] F.G. Caballero, H.K.D.H. Bhadeshia, K.J.A. Mawella, D.G. Jones, P. Brown, Design of novel high strength bainitic steels: Part 1, Mater. Sci. Technol. 17 (2001) 512–516. https://doi.org/10.1179/026708301101510348.
[44] C. Garcia-Mateo, F.G. Caballero, Design of carbide-free low-temperature ultra high strength bainitic steels, Int. J. Mater. Res. 98 (2007) 137–143. https://doi.org/10.3139/146.101440.
[45] F.G. Caballero, M.K. Miller, C. Garcia-Mateo, J. Cornide, M.J. Santofimia, Temperature dependence of carbon supersaturation of ferrite in bainitic steels, Scr. Mater. 67 (2012) 846–849. https://doi.org/10.1016/j.scriptamat.2012.08.007.
[46] E. Kozeschnik, H.K.D.H. Bhadeshia, Influence of silicon on cementite precipitation in steels, Mater. Sci. Technol. 24 (2008) 343–347. https://doi.org/10.1179/174328408X275973.
[47] H.K.D.H. Bhadeshia, The first bulk nanostructured metal, Sci. Technol. Adv. Mater. 14 (2013) 014202. https://doi.org/10.1088/1468-6996/14/1/014202.
[48] M. Muniz-Mangas, Welding of bainitic rail steels, University of Sheffield, 2017.

[49] Goldschmidt, Technical presentation of SoW-5 welding process, (n.d.). https://www.gt-railservice.com/fileadmin/user_upload/PDF/Schienenverbindung/SOW-5_DE-EN-FR.pdf (accessed October 26, 2020).
[50] B. Beausir and J.-J. Fundenberger, Analysis Tools for Electron and X-ray diffraction, ATEX - software, www.atex-software.eu, Université de Lorraine - Metz, 2017, (n.d.).
[51] R. Devanathan, P. Clayton, Rolling-sliding wear behavior of three bainitic steels, Wear. 151 (1991) 255–267. https://doi.org/10.1016/0043-1648(91)90253-Q.
[52] L. Yajiang, W. Juan, L. Peng, Fine structure in the inter-critical heat-affected zone of HQ130 super-high strength steel, Bull. Mater. Sci. 26 (2003) 273–278. https://doi.org/10.1007/BF02707803.
[53] M. Eroğlu, M. Aksoy, Effect of initial grain size on microstructure and toughness of intercritical heat-affected zone of a low carbon steel, Mater. Sci. Eng. A. 286 (2000) 289–297. https://doi.org/10.1016/S0921-5093(00)00801-7.
[54] E. Bonnevie, G. Ferrière, A. Ikhlef, D. Kaplan, J.M. Orain, Morphological aspects of martensite–austenite constituents in intercritical and coarse grain heat affected zones of structural steels, Mater. Sci. Eng. A. 385 (2004) 352–358. https://doi.org/10.1016/j.msea.2004.06.033.
[55] Y. Wang, R. Kannan, L. Li, Correlation Between Intercritical Heat-Affected Zone and Type IV Creep Damage Zone in Grade 91 Steel, Metall. Mater. Trans. A. 49 (2018) 1264–1275. https://doi.org/10.1007/s11661-018-4490-x.
[56] Z. Li, X. Zhao, D. Shan, Impact Toughness of Subzones in the Intercritical Heat-Affected Zone of Low-Carbon Bainitic Steel, Materials. 11 (2018) 959. https://doi.org/10.3390/ma11060959.
[57] X. Gui, K. Wang, G. Gao, R.D.K. Misra, Z. Tan, B. Bai, Rolling contact fatigue of bainitic rail steels: The significance of microstructure, Mater. Sci. Eng. A. 657 (2016) 82–85. https://doi.org/10.1016/j.msea.2016.01.052.
[58] B. Liu, W. Li, X. Lu, X. Jia, X. Jin, The effect of retained austenite stability on impact-abrasion wear resistance in carbide-free bainitic steels, Wear. 428–429 (2019) 127–136. https://doi.org/10.1016/j.wear.2019.02.032.
[59] A. Kumar, A. Singh, Microstructural effects on the sub-critical fatigue crack growth in nano-bainite, Mater. Sci. Eng. A. 743 (2019) 464–471. https://doi.org/10.1016/j.msea.2018.11.114.
[60] A. Kumar, A. Dutta, S.K. Makineni, M. Herbig, R.H. Petrov, J. Sietsma, In-situ observation of strain partitioning and damage development in continuously cooled carbide-free bainitic steels using micro digital image correlation, Mater. Sci. Eng. A. 757 (2019) 107–116. https://doi.org/10.1016/j.msea.2019.04.098.
[61] Y. Shen, S.M. Moghadam, F. Sadeghi, K. Paulson, R.W. Trice, Effect of retained austenite – Compressive residual stresses on rolling contact fatigue life of carburized AISI 8620 steel, Int. J. Fatigue. 75 (2015) 135–144. https://doi.org/10.1016/j.ijfatigue.2015.02.017.
[62] J.P. Liu, Y.Q. Li, Q.Y. Zhou, Y.H. Zhang, Y. Hu, L.B. Shi, W.J. Wang, F.S. Liu, S.B. Zhou, C.H. Tian, New insight into the dry rolling-sliding wear mechanism of carbide-free bainitic and pearlitic steel, Wear. 432–433 (2019) 202943. https://doi.org/10.1016/j.wear.2019.202943.
[63] K. Sugimoto, T. Iida, J. Sakaguchi, T. Kashima, Retained Austenite Characteristics and Tensile Properties in a TRIP Type Bainitic Sheet Steel., ISIJ Int. 40 (2000) 902–908. https://doi.org/10.2355/isijinternational.40.902.
[64] R.H. Leal, Transformation toughening of metastable austenitic steels, Thesis, Massachusetts Institute of Technology, 1984. https://dspace.mit.edu/handle/1721.1/15349 (accessed January 21, 2020).
[65] R. Rementeria, L. Morales-Rivas, M. Kuntz, C. Garcia-Mateo, E. Kerscher, T. Sourmail, F.G. Caballero, On the role of microstructure in governing the fatigue behaviour of nanostructured bainitic steels, Mater. Sci. Eng. A. 630 (2015) 71–77. https://doi.org/10.1016/j.msea.2015.02.016.
[66] G.T.C. Ooi, S. Roy, S. Sundararajan, Investigating the effect of retained austenite and residual stress on rolling contact fatigue of carburized steel with XFEM and experimental approaches, Mater. Sci. Eng. A. 732 (2018) 311–319. https://doi.org/10.1016/j.msea.2018.06.078.
[67] Z. Dong, W.F. Xing, C.Q. Gong, Z.M. Xin, C.Y. Quian, Effect of retained austenite on rolling element fatigue and its mechanism, Wear. 105 (1985) 223–234. https://doi.org/10.1016/0043-1648(85)90069-9.

[68] C. Xie, Z. Liu, X. He, X. Wang, S. Qiao, Effect of martensite–austenite constituents on impact toughness of pre-tempered MnNiMo bainitic steel, Mater. Charact. 161 (2020) 110139. https://doi.org/10.1016/j.matchar.2020.110139.